J Physiol 603.17 (2025) pp 4785–4816

Spine apparatus modulates Ca^{2+} in spines through spatial localization of sources and sinks

M. Hernández Mesa[1], G. C. Garcia[2], F. J. Hoerndli[3], K. J. McCabe[1] and P. Rangamani[4]

[1]*Department of Computational Physiology, Simula Research Laboratory, Oslo, Norway*
[2]*Computational Neurobiology Laboratory, Salk Institute for Biological Studies, La Jolla, California, USA*
[3]*Department of Biomedical Sciences, Colorado State University, Fort Collins, Colorado, USA*
[4]*Department of Mechanical and Aerospace Engineering, University of California San Diego, San Diego, California, USA*

Handling Editors: Katalin Toth & Jean-Claude Béïque

The peer review history is available in the Supporting Information section of this article (https://doi.org/10.1113/JP286859#support-information-section).

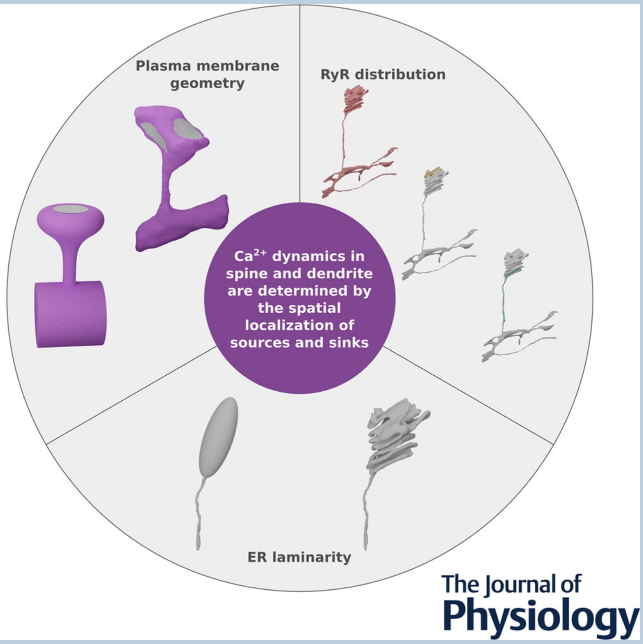

Abstract figure legend Factors governing the dynamics of Ca^{2+} in dendritic spines include plasma membrane geometry, RyR distribution and ER laminarity.

María Hernandez Mesa received her PhD in Informatics from the University of Oslo in 2024. Under the supervision of Kimberly McCabe and Padmini Rangamani, she explored the interplay between receptor clustering, membrane morphology, and calcium signaling in excitable cells using computational models. As part of the SUURPh program, she conducted research at the University of California San Diego in the Rangamani lab. Her work focuses on employing computational tools to understand intracellular biophysical properties.

This article was first published as a preprint. Herńandez Mesa M, Garcia GC, Hoerndli FJ, McCabe KJ, Rangamani P. 2023. Spine apparatus modulates Ca2+ in spines through spatial localization of sources and sinks. bioRxiv. https://doi.org/10.1101/2023.09.22.558941

DOI: 10.1113/JP286859

Abstract Dendritic spines are small protrusions on dendrites in neurons and serve as sites of postsynaptic activity. Some of these spines contain smooth endoplasmic reticulum (SER), and sometimes an even further specialized SER known as the spine apparatus (SA). In this work we developed a stochastic spatial model to investigate the role of the SER and the SA in modulating Ca^{2+} dynamics. Using this model, we investigated how ryanodine receptor (RyR) localization, IP_3R localization, spine membrane geometry and SER geometry can impact Ca^{2+} transients in the spine and in the dendrite. Our simulations found that RyR opening is dependent on its location in the SER and on the SER geometry. To maximize Ca^{2+} in the dendrites (for activating clusters of spines and spine-to-spine communication), a laminar SA was favourable with RyRs localized in the neck region, closer to the dendrite. Furthermore locating the IP_3Rs in the dendrite, as measured experimentally, also increases Ca^{2+} in the dendrite. We also found that the presence of the SER without the laminar structure, coupled with RyR localization at the head, leads to higher Ca^{2+} presence in the spine. These predictions serve as design principles for understanding how spines with an ER can regulate Ca^{2+} dynamics differently from spines without ER through a combination of geometry and receptor localization.

(Received 3 May 2024; accepted after revision 23 June 2025; first published online 11 August 2025)

Corresponding author P. Rangamani: Department of Mechanical and Aerospace Engineering, University of California San Diego, San Diego, California, 92093, USA. Email: prangamani@ucsd.edu

Key points

- Ca^{2+} transients in the spine are characterized by the interplay among membrane receptors, RyRs, SERCA, and IP_3Rs.
- Here we build a spatial, particle-based stochastic model that integrates these components to study how the spine apparatus and receptor localization affect Ca^{2+} signaling.
- Our results show that positioning RyRs near the neck of the spine apparatus enhances spine-to-dendrite communication.
- Additionally, our model highlights the importance of membrane curvature and spine apparatus shape for Ca^{2+} signaling within dendritic spines.

Significance statement

Dendritic spines are small protrusions along the dendrite that allow for neuronal communication at synapses. A stimulus from the presynaptic neuron, which is relevant to learning and memory formation, results in a Ca^{2+} increase at the dendritic spines. How are the Ca^{2+} dynamics regulated by the organelles and receptors in the spine? In this work we develop a spatial, particle-based model that integrates spatial and biochemical components of Ca^{2+} dynamics in spines to answer this question. Using this model, we found that how the sources and sinks are organized in a single spine can affect the spatiotemporal dynamics of calcium. Our findings shed light on how spatial organization of receptors and organelles can play a critical role in neuronal function.

Introduction

Communication between two neurons occurs at the synapse, which consists of three parts: a presynaptic terminal on one neuron, the postsynaptic site of another neuron and the synaptic cleft between them. Dendritic spines are small protrusions (0.04–0.29 μm^3, Harris et al. 1992; Spacek & Harris 1997) located along the dendrite of the neuron receiving the signal (postsynaptic sites). The biochemical machinery initiated by the release of neurotransmitters activates multiple biochemical reactions within the spines (Colgan & Yasuda, 2014), which play an important role in learning and memory formation (Bell et al., 2022). Dendritic spines are highly dynamic structures, capable of changing their size and shape in response to synaptic activity (Nimchinsky et al., 2002; Rangamani et al., 2016; Yang et al., 2009), and these alterations may affect learning and memory formation (Matsuzaki et al., 2004; Van Harreveld & Fifkova, 1975). Spines also come in different shapes and sizes, and spine geometry is thought to impact synaptic plasticity (Alimohamadi et al., 2021; Bell et al., 2022, 2019; Harris et al., 1992; Ohadi et al., 2019). Ca^{2+} dynamics are a key determinant of learning and memory formation in spines as they regulate several mechanisms such as the activation of Ca^{2+}sensitive proteins as Ca^{2+}/calmodulin-dependent kinase type II (CaMKII), synaptic plasticity and synapse-to-nucleus communication (Bading, 2013; Higley & Sabatini, 2012).

Synaptic Ca^{2+} signals are generated upon membrane depolarization as a response to the release of glutamate from the presynaptic terminal (Bading, 2013). This allows for the activation of N-methyl-D-aspartate receptors (NMDAR) resulting in an influx of Ca^{2+}. The voltage-sensitive Ca^{2+}channels (VSCC) located on the plasma membrane of dendritic spines are an additional source for cytosolic Ca^{2+}. In response to this Ca^{2+} influx, plasma membrane Ca^{2+}-ATPase (PMCA) pumps and Na^{+}–Ca^{2+} exchangers (NCX) remove the cytosolic Ca^{2+} out of the spine (Fig. 1*A*). Intracellular Ca^{2+} stores can also modulate the levels of cytosolic Ca^{2+} concentrations, for example, the endoplasmic reticulum (ER), which is the largest intracellular Ca^{2+} storage organelle in eukaryotic cells (Lam & Galione, 2013) (see Fig. 1*A*). In addition, a subset of dendritic spines (around 48% of adult spines) contains smooth endoplasmic reticulum (SER) (Spacek & Harris, 1997). A specialized form of the SER, called the spine apparatus (SA) (Bourne & Harris, 2008; Jedlicka et al., 2008), is identified by its characteristic laminar structure of stacked SA discs (Bourne & Harris, 2008) and is found in about 10%–20% of adult spines (Spacek & Harris, 1997). Spacek and Harris (1997) showed that the presence of SA is more prevalent in mature mushroom-shaped spines. The actin-associated protein synaptopodin is necessary for SA formation as it localizes to the F-actin matrix in between the SA discs (Konietzny et al., 2022). Due to its capacity for storing Ca^{2+}, the SA, which was first observed by Vlachos et al. (2009), has been suggested to play an important role in

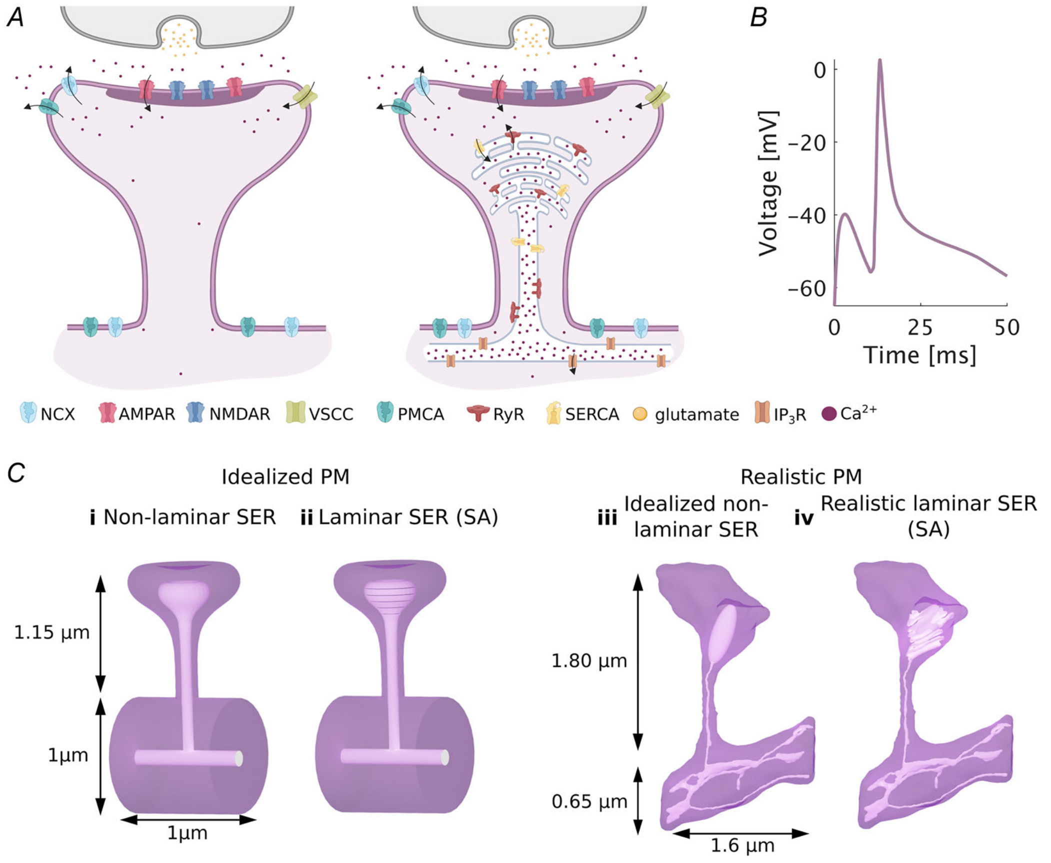

Figure 1. Overview of the model and geometries used to investigate the role of the SER and spine apparatus in regulating Ca^{2+} dynamics
(A) Schematic of the molecular components, currents and receptors included in this model. On the left, the spine apparatus is not included. On the right, a spine apparatus with RyRs and SERCA is included in the spine. The shaded part at the spines represents the postsynaptic density (PSD). This panel was generated using *Biorender.com*. (B) The stimulus is modelled as glutamate release coupled with a simultaneous change in membrane potential characterized by an excitatory postsynaptic potential (EPSP) and a back-propagating action potential (bAP) as described in Bell et al. (2022) and Bartol et al. (2015). (C) The four different geometries used in this work consider both an idealized (Alimohamadi et al., 2021) and a realistic plasma membrane generated from experimental images (Wu et al., 2017), along with a non-laminar SER and a laminar SER representing the SA.

synaptic plasticity and Ca^{2+} signalling (Jedlicka et al., 2008; Konietzny et al., 2022). Ca^{2+} is stored in the SA via the sarco/ER Ca^{2+}-ATPase (SERCA) pump, whereas Ca^{2+} is released from the SA through the inositol 1,4,5 triphosphate receptor (IP_3R) and the ryanodine receptor (RyR). Cytosolic Ca^{2+} ions activate RyRs, which allows for further Ca^{2+} release into the cytosol, a process known as Ca^{2+}-induced Ca^{2+} release (CICR). Although IP_3 is the principal agonist of IP_3Rs, some studies have suggested that IP_3Rs also play a role in CICR (Berridge, 1993; Barbara, 2002).

The localization of these receptors varies within the brain, with IP_3Rs being more prevalent in dendritic shafts and RyRs more common in dendritic spines, as shown by Sharp et al. using immunohistochemistry (Sharp et al., 1993; Segal & Korkotian, 2014). Although the effect of IP_3Rs on plasticity has been extensively studied (de Sevilla et al., 2008; de Sevilla & Buno, 2010; Segal & Korkotian, 2014), the role of RyRs on synaptic plasticity remains to be fully explored. Korkotian and Segal have studied the role of the SA in Ca^{2+} dynamics using flashed photolysis of caged Ca^{2+} inside dendritic spines (Korkotian & Segal, 2011; Segal & Korkotian, 2014). They observed a second peak of cytosolic Ca^{2+} in spines with SA after flash photolysis of caged Ca^{2+} in dendritic spines; this second peak was not present in those spines lacking SA. When an RyR antagonist was used, the second peak was abolished in SA-containing spines (Korkotian & Segal, 2011; Segal & Korkotian, 2014). RyR localization within dendritic spines has been recently studied. Vlachos et al. (2009) showed experimentally the colocalization of the RyRs with synaptopodin whereas Basnayake et al. (2019) showed using super-resolution stimulated emission depletion imaging, in both cultured rat neurons and mouse hippocampal brain slices, that RyRs tend to be located on the lower part of the SA towards the base of the spine neck. However the exact contribution of the SER, the SA and the localized pools of RyRs to synaptic plasticity and Ca^{2+} dynamics in intracellular signalling remains unclear (Segal et al., 2010).

Computational models can augment our understanding of the role of the SA and the RyRs on Ca^{2+} dynamics in dendritic spine communication. Breit et al. (2018) used a deterministic model to establish the importance of an SA with Ca^{2+} releasing receptors (RyRs and IP_3Rs) in order for Ca^{2+} to reach the dendrites and thus allow spine-to-dendrite communication. Due to the small volume of spines, the use of stochastic models including particle diffusion instead of deterministic models has been deemed preferable (Bartol et al., 2015; Bhalla, 2004; Holcman et al., 2004; Kotaleski & Blackwell, 2010). Therefore, Bell et al. (2022) used a stochastic model to study the effect of spine shape and SER morphology on synaptic weight. Bell et al. (2022) used a physiological stimulus based on glutamate release from a presynaptic terminal and membrane depolarization to investigate how the volume-to-surface area of the spine modulates changes in synaptic strength on both spines without SER and on spines containing a passive SER. Separately Basnayake et al. (2019) also included stochastic simulations to show that more Ca^{2+} reaches the dendrite when the RyRs are located towards the lower part of the SA.

These studies highlight open questions about the impact of spine geometry, SER and SA geometry, and RyR localization on Ca^{2+} dynamics in spines and dendrites. For example, how does RyR localization on the SER affect Ca^{2+} dynamics? What configurations of SER geometry and RyR localization give rise to increased Ca^{2+} in the spine head? In the dendrite? To investigate the crosstalk between the geometric features listed above and Ca^{2+} dynamics, we developed a stochastic computational model of the main molecular components in spines with a focus on RyR-mediated CICR. In our model we considered the role of RyR clustering inspired by work in cardiomyocytes (Hernández Mesa et al., 2022; Kolstad et al., 2018; Shen et al., 2019) and the role of RyR localization based on experimental observations (Basnayake et al., 2019). As the ER and the spine have unique shapes (Alimohamadi et al., 2021; Bourne & Harris, 2008; Jedlicka et al., 2008), we also investigated how the geometries of both the spine head and the ER (non-laminar and SA) could impact the RyR- and IP_3Rdriven Ca^{2+} dynamics using idealized and realistic geometries. Our simulations reveal complex rules for Ca^{2+} handling in dendritic spines and dendrites, foremost among which is that spine geometry and SA laminarity, in combination with receptor localization, govern RyR- and IP_3R-mediated Ca^{2+} dynamics in spine heads and dendrites. This interplay is also affected by SERCA dynamics and Ca^{2+} buffering, which play important roles in modulating Ca^{2+} in spines and in dendrites. Taken together, these results provide novel insights into geometrical nuances and transport phenomena that ultimately affect downstream signal propagation in neurons.

Model development

In this work we developed a stochastic spatial particle-based model that incorporates RyR dynamics into a previously described Ca^{2+} framework (Bell et al., 2022; Bartol et al., 2015). In the following section, we explain the details, methods and assumptions taken with regard to model development. The receptors and channels considered in the model are depicted in Fig. 1*A*. This section is divided as follows: first, we describe the equations used for the receptors at the plasma membrane. Then we explain the equations in the cytosol and those used for describing the receptors used in the ER/SA.

In the last two sections, we describe the geometries used in this work, followed by the stimulus and further simulation details. An overview of all the equations used is given in Tables 1 and 3, and in Section 4.3.1 for the RyR equations. The parameters used are summarized in Table 2. The model was implemented in the spatial, stochastic, particle-based framework MCell4 (Husar et al., 2022) to capture the stochasticity due to particle diffusion in small volumes such as spines. As most of the equations were derived from Bell et al. (2022), who developed their model using MCell3, we compared their results with our implementation of the model in the latest version of MCell to ensure that the results matched. In addition, an ODE version was implemented in MATLAB Inc. (2022) to allow for the optimization of specific global parameters.

Receptors at the plasma membrane

Most of the plasma membrane transport mechanisms and equations are described in Bell et al. (2022). For completeness, in the following sections, a brief description for each module is given.

NMDAR receptors. As in Bell et al. (2022), we assume the NMDAR model proposed by Vargas-Caballero and Robinson (2004). The model equations and kinetic rates are obtained from Vargas-Caballero and Robinson (2004) and shown in Tables 1 and 2, respectively. A schematic of the NMDAR reaction rate model is given in Fig. 5*B*. The NMDARs are located in the postsynaptic density (PSD) with surface density of 150 μm^{-2}. As described in Bell et al. (2022), Ca^{2+} influx into the cytosol through open NMDARs is determined by the following reaction:

$$\mathrm{NMDAR} \xrightarrow{k_{\mathrm{N}}(\mathrm{V})} \mathrm{NMDAR} + \mathrm{Ca}^{2+}_{\mathrm{cyto}}\,, \tag{1}$$

where $k_{\mathrm{N}}(\mathrm{V})$ is a voltage-dependent rate given by the following expression:

$$k_{\mathrm{N}}(\mathrm{V}) = \gamma_{\mathrm{NMDAR}} \cdot \frac{V_{\mathrm{m}}(\mathrm{t}) - V_{\mathrm{r}}}{2 \cdot q_{\mathrm{e}}}\,, \tag{2}$$

where q_{e} is the elementary charge. Two further reaction rates, $k_{\mathrm{U}}(\mathrm{V})$ and $k_{\mathrm{B}}(\mathrm{V})$, which represent the change between the states NMDAR and NMDAR$_{\mathrm{B}}$ are also dependent on the transmembrane potential (Fig. 1*B*) and as in Bartol et al. (2015) are given by the following expressions:

$$k_{\mathrm{U}}(\mathrm{V}) = 10800 \cdot \exp\left(\frac{V_{\mathrm{m}}(\mathrm{t})}{47}\right), \tag{3}$$

$$k_{\mathrm{B}}(\mathrm{V}) = 1200 \cdot \exp\left(\frac{-V_{\mathrm{m}}(\mathrm{t})}{17}\right). \tag{4}$$

Table 1. Chemical reactions used in the model, with the exception of the RyR equations, which are listed in Section 4.3.1. For clarity in the table, abbreviated reference labels are used: reactions marked VC are from Vargas-Caballero and Robinson (2004), J from Jonas et al. (1993), Ba from Bartol et al. (2015) and Be from Bell et al. (2022)

Reactions for NMDAR	**Ref.**
$\mathrm{NMDAR}_0 + \mathrm{glut.} \xrightleftharpoons[\mathrm{k}_{\mathrm{N,C1C0}}]{\mathrm{k}_{\mathrm{N,C0C1}}} \mathrm{NMDAR}_1$	VC
$\mathrm{NMDAR}_1 + \mathrm{glut.} \xrightleftharpoons[\mathrm{k}_{\mathrm{N,C2C1}}]{\mathrm{k}_{\mathrm{N,C1C2}}} \mathrm{NMDAR}_2$	VC
$\mathrm{NMDAR}_2 \xrightleftharpoons[\mathrm{k}_{\mathrm{DC2}}]{\mathrm{k}_{\mathrm{C2D}}} \mathrm{NMDAR}_D$	VC
$\mathrm{NMDAR}_2 \xrightleftharpoons[\mathrm{k}_{\mathrm{N,0C2}}]{\mathrm{k}_{\mathrm{N,C20}}} \mathrm{NMDAR}$	VC
$\mathit{NMDAR} \xrightarrow{\mathrm{k}_{\mathrm{N}}(V_{\mathrm{m}})} \mathrm{NMDAR} + \mathrm{Ca}^{2+}_{\mathrm{cyto}}$	VC
$\mathrm{NMDAR}_B \xrightleftharpoons[\mathrm{k}_{\mathrm{B}}(V_{\mathrm{m}})]{\mathrm{k}_{\mathrm{U}}(V_{\mathrm{m}})} \mathit{NMDAR}$	VC
$\mathrm{NMDAR}_{2B} \xrightleftharpoons[\mathrm{k}_{\mathrm{0C2}b}]{\mathrm{k}_{\mathrm{C20b}}} \mathrm{NMDAR}_B$	VC
$\mathrm{NMDAR}_{2B} \xrightleftharpoons[\mathrm{k}_{\mathrm{DC2}}]{\mathrm{k}_{\mathrm{C2D}}} \mathrm{NMDAR}_{\mathrm{DB}}$	VC
$\mathrm{NMDAR}_{1B} + \mathrm{glut.} \xrightleftharpoons[\mathrm{k}_{\mathrm{N,C2C1}}]{\mathrm{k}_{\mathrm{N,C1C2}}} \mathrm{NMDAR}_{2B}$	VC
$\mathrm{NMDAR}_{0B} + \mathrm{glut.} \xrightleftharpoons[\mathrm{k}_{\mathrm{N,C1C0}}]{\mathrm{k}_{\mathrm{N,C0C1}}} \mathrm{NMDAR}_{1B}$	VC
Reactions for AMPAR	**Ref.**
$\mathit{AMPAR}_0 + \mathrm{glut.} \xrightleftharpoons[\mathrm{k}_{\mathrm{A,C1C0}}]{\mathrm{k}_{\mathrm{A,C0C1}}} \mathrm{AMPAR}_1$	J
$\mathrm{AMPAR}_1 + \mathrm{glut.} \xrightleftharpoons[\mathrm{k}_{\mathrm{A,C2C1}}]{\mathrm{k}_{\mathrm{A,C1C2}}} \mathrm{AMPAR}_2$	J
$\mathrm{AMPAR}_2 \xrightleftharpoons[\mathrm{k}_{\mathrm{A,C02}}]{\mathrm{k}_{\mathrm{A,C20}}} \mathrm{AMPAR}$	J
$\mathrm{AMPAR}_1 \xrightleftharpoons[\mathrm{k}_{\mathrm{C3C1}}]{\mathrm{k}_{\mathrm{C1C3}}} \mathrm{AMPAR}_3$	J
$\mathrm{AMPAR}_3 + \mathrm{glut.} \xrightleftharpoons[\mathrm{k}_{\mathrm{C4C3}}]{\mathrm{k}_{\mathrm{C3C4}}} \mathrm{AMPAR}_4$	J
$\mathrm{AMPAR}_2 \xrightleftharpoons[\mathrm{k}_{\mathrm{C4C2}}]{\mathrm{k}_{\mathrm{C2C4}}} \mathrm{AMPAR}_4$	J
$\mathrm{AMPAR}_4 \xrightleftharpoons[\mathrm{k}_{\mathrm{C5C4}}]{\mathrm{k}_{\mathrm{C4C5}}} \mathrm{AMPAR}_5$	J
$\mathrm{AMPAR}_5 \xrightleftharpoons[\mathrm{k}_{\mathrm{0C5}}]{\mathrm{k}_{\mathrm{C50}}} \mathrm{AMPAR}$	J
Reactions for VSCC	**Ref.**
$\mathrm{VSCC}_0 \xrightleftharpoons[b_1(V_{\mathrm{m}})]{a_1(V_{\mathrm{m}})} \mathrm{VSCC}_1$	Ba
$\mathrm{VSCC}_1 \xrightleftharpoons[b_2(V_{\mathrm{m}})]{a_2(V_{\mathrm{m}})} \mathrm{VSCC}_2$	Ba
$\mathrm{VSCC}_2 \xrightleftharpoons[b_3(V_{\mathrm{m}})]{a_3(V_{\mathrm{m}})} \mathrm{VSCC}_3$	Ba
$\mathrm{VSCC}_3 \xrightleftharpoons[b_4(V_{\mathrm{m}})]{a_4(V_{\mathrm{m}})} \mathrm{VSCC}$	Ba
$\mathrm{VSCC} \xrightarrow{\mathrm{k}_{\mathrm{Ca}}(V_{\mathrm{m}})} \mathrm{VSCC} + \mathrm{Ca}^{2+}_{\mathrm{cyto}}$	Ba

(*Continued*)

Table 1. (Continued)

Reactions for PMCA	Ref.
$Ca^{2+}_{cyto} + PMCA \underset{k_{P2}}{\overset{k_{P1}}{\rightleftharpoons}} PMCA_1$	Ba
$PMCA_1 \xrightarrow{k_{P3}} PMCA$	Ba
$PMCA \xrightarrow{k_{P,leak}} PMCA + Ca^{2+}_{cyto}$	Ba
Reactions for NCX	**Ref.**
$Ca^{2+}_{cyto} + NCX \underset{k_{N2}}{\overset{k_{N1}}{\rightleftharpoons}} NCX_1$	Ba
$NCX_1 \xrightarrow{k_{N3}} NCX$	Ba
$NCX \xrightarrow{k_{N,leak}} NCX + Ca^{2+}_{cyto}$	Ba
Reactions for Ca^{2+} buffers	**Ref.**
$Ca^{2+}_{cyto} + B_f \underset{k_{Bf,off}}{\overset{k_{Bf,on}}{\rightleftharpoons}} CaB_f$	Be
$Ca^{2+}_{cyto} + B_m \underset{k_{Bm,off}}{\overset{k_{Bm,on}}{\rightleftharpoons}} CaB_m$	Be
Reactions for Ca^{2+} decay	**Ref.**
$Ca^{2+}_{cyto} \xrightarrow{k_d} \emptyset$	Be
Reactions for SERCA	**Ref.**
$SERCA_x + Ca^{2+}_{cyto} \underset{k_{x1x0}}{\overset{k_{x0x1}}{\rightleftharpoons}} SERCA_{x1}$	Ba
$SERCA_{x1} + Ca^{2+}_{cyto} \underset{k_{x2x1}}{\overset{k_{x1x2}}{\rightleftharpoons}} SERCA_{x2}$	Ba
$SERCA_{x2} \underset{k_{y2x2}}{\overset{k_{x2y2}}{\rightleftharpoons}} SERCA_{y2}$	Ba
$SERCA_{y2} \underset{k_{y1y2}}{\overset{k_{y2y1}}{\rightleftharpoons}} SERCA_{y1} + Ca^{2+}_{ER}$	Ba
$SERCA_{y1} \underset{k_{y0y1}}{\overset{k_{y1y0}}{\rightleftharpoons}} SERCA_y + Ca^{2+}_{ER}$	Ba
$SERCA_y \underset{k_{x0y0}}{\overset{k_{y0x0}}{\rightleftharpoons}} SERCA_x$	Ba
$Ca^{2+}_{ER} \xrightarrow{k_{S,leak}} Ca^{2+}_{cyto}$	Be

AMPAR receptors. It has been shown that 90% of hippocampal neurons contain GluA2 subunit (Wenthold et al., 1996), which characterizes the impermeability of α-amino-3-hydroxy-5-methyl-4-isoxazolepropionic acid receptors (AMPARs) to Ca^{2+}. Therefore our model does not include Ca^{2+} flux through AMPARs. Rather AMPARs serve as glutamate buffers to simulate glutamate binding competition with NMDARs. The model of Jonas et al. (1993) was used to simulate the binding of glutamate to AMPAR. We assumed an AMPAR density of 1200 μm^{-2} as described in Bartol et al. (2015) and Bell et al. (2022). AMPAR receptors were located only at the PSD.

Table 2. Reaction rates and parameters used for the simulation. For clarity in the table, abbreviated reference labels are used: reactions marked Ba from Bartol et al. (2015), Be from Bell et al. (2022), Ta from Tanskanen et al. (2007) and Doi from Doi et al. (2005)

	Parameters for NMDAR	
Name	**Value**	**Ref.**
$k_{N,C0C1}$	$2 \cdot 10^7\ (Ms)^{-1}$	Ba
$k_{N,C1C0}$	$11\ s^{-1}$	Ba
$k_{N,C1C2}$	$1 \cdot 10^7\ (Ms)^{-1}$	Ba
$k_{N,C2C1}$	$22\ s^{-1}$	Ba
k_{C2D}	$16.8\ s^{-1}$	Ba
k_{DC2}	$3.6\ s^{-1}$	Ba
$k_{N,C20}$	$93\ s^{-1}$	Ba
$k_{N,0C2}$	$183.2\ s^{-1}$	Ba
k_{C20b}	$97\ s^{-1}$	Ba
k_{0C2b}	$574\ s^{-1}$	Ba
$k_N(V)$	$\gamma_N \cdot \frac{V_m(t)-V_r}{2 \cdot q_e} s^{-1}$	Be
γ_N	$4.5 \cdot 10^{-15}\ S$	Be
V_r	$3\ mV$	Be
$k_U(V)$	$10,800 \cdot \exp\left(\frac{V_m(t)}{47}\right) s^{-1}$	Ba
$k_B(V)$	$1200 \cdot \exp\left(\frac{-V_m(t)}{17}\right) s^{-1}$	Ba
	Parameters for AMPAR	
Name	**Value**	**Ref.**
$k_{A,C0C1}$	$9.18 \cdot 10^6\ (Ms)^{-1}$	Ba
$k_{A,C1C0}$	$8520\ s^{-1}$	Ba
$k_{A,C1C2}$	$5.68 \cdot 10^7\ (Ms)^{-1}$	Ba
$k_{A,C2C1}$	$6520\ s^{-1}$	Ba
$k_{A,C20}$	$8480\ s^{-1}$	Ba
$k_{A,C02}$	$1800\ s^{-1}$	Ba
k_{C1C3}	$5780\ s^{-1}$	Ba
k_{C3C1}	$78.4\ s^{-1}$	Ba
k_{C3C4}	$2.54 \cdot 10^6\ (Ms)^{-1}$	Ba
k_{C4C3}	$91.4\ s^{-1}$	Ba
k_{C2C4}	$344\ s^{-1}$	Ba
k_{C4C2}	$1.45\ s^{-1}$	Ba
k_{C4C5}	$33.6\ s^{-1}$	Ba
k_{C5C4}	$380.8\ s^{-1}$	Ba
k_{0C5}	$35.4\ s^{-1}$	Ba
k_{C50}	$8\ s^{-1}$	Ba
	Parameters for VSCC	
Name	**Value**	**Ref.**
$a_i(V)$	$\alpha_i \cdot \exp\left(\frac{V_m(t)}{V_i}\right)$	Ba
$b_i(V)$	$\beta_i \cdot \exp\left(\frac{V_m(t)}{V_i}\right)$	Ba
α_1	$8080\ s^{-1}$	Ba
α_2	$13,400\ s^{-1}$	Ba
α_3	$8780\ s^{-1}$	Ba
α_4	$34,700\ s^{-1}$	Ba
β_1	$5760\ s^{-1}$	Ba
β_2	$12,600\ s^{-1}$	Ba

(*Continued*)

Table 2. (Continued)

Parameters for VSCC

Name	Value	Ref.
β_3	$163,00\ \mathrm{s}^{-1}$	Ba
β_4	$3680\ \mathrm{s}^{-1}$	Ba
V_1	49.14 mV	Ba
V_2	42.08 mV	Ba
V_3	55.31 mV	Ba
V_4	26.55 mV	Ba

Parameters for PMCA

Name	Value	Ref.
k_{P1}	$1.5 \cdot 10^8\ (\mathrm{Ms})^{-1}$	Ba
k_{P2}	$15\ \mathrm{s}^{-1}$	Ba
k_{P3}	$12\ \mathrm{s}^{-1}$	Ba
$k_{P,leak}$	$4.3\ \mathrm{s}^{-1}$	Ba

Parameters for NCX

Name	Value	Ref.
k_{N1}	$3 \cdot 10^8\ (\mathrm{Ms})^{-1}$	Ba
k_{N2}	$300\ \mathrm{s}^{-1}$	Ba
k_{N3}	$600\ \mathrm{s}^{-1}$	Ba
$k_{N,leak}$	$19.4\ \mathrm{s}^{-1}$	Ba

Parameters for Ca^{2+} buffers

Name	Value	Ref.
$k_{Bf,on}$	$1 \cdot 10^6\ (\mathrm{Ms})^{-1}$	Ba
$k_{Bf,off}$	$2\ \mathrm{s}^{-1}$	Ba
$k_{Bm,on}$	$1 \cdot 10^6\ (\mathrm{Ms})^{-1}$	Ba
$k_{Bm,off}$	$1\ \mathrm{s}^{-1}$	Ba

Parameters for Ca^{2+} decay

Name	Value	Ref.
k_d	$50\ \mathrm{s}^{-1}$	optim.

Parameters for SERCA

Name	Value	Ref.
k_{x0x1}	$2 \cdot 10^8\ (\mathrm{Ms})^{-1}$	Ba
k_{x1x0}	$83.7\ \mathrm{s}^{-1}$	Ba
k_{x1x2}	$1 \cdot 10^8\ (\mathrm{Ms})^{-1}$	Ba
k_{x2x1}	$167.4\ \mathrm{s}^{-1}$	Ba
k_{x2y2}	$0.6\ \mathrm{s}^{-1}$	Ba
k_{y2x2}	$0.097\ \mathrm{s}^{-1}$	Ba
k_{x0y0}	$1.2 \cdot 10^{-3}\ \mathrm{s}^{-1}$	Ba
k_{y0x0}	$0.4\ \mathrm{s}^{-1}$	Ba
k_{y0y1}	$12\ \mathrm{s}^{-1}$	Ba
k_{y1y0}	$30.02\ \mathrm{s}^{-1}$	Ba
k_{y1y2}	$6\ \mathrm{s}^{-1}$	Ba
k_{y2y1}	$60.04\ \mathrm{s}^{-1}$	Ba
$k_{S,leak}$	$0.1608\ \mathrm{s}^{-1}$	optim.

(*Continued*)

Table 2. (Continued)

Parameters for RyR

Name	Value	Ref.
α	$650\ \mathrm{s}^{-1}$	Ta
β	$60\ \mathrm{s}^{-1}$	Ta
γ	$5\ \mathrm{s}^{-1}$	Ta
δ	$75\ \mathrm{s}^{-1}$	Ta
δ'	$600\ \mathrm{s}^{-1}$	Ta
k_{IO}	$250,000\ \mathrm{s}^{-1}$	Ta
k_{IC}	$450,000\ \mathrm{s}^{-1}$	Ta
k_{IU}	$1\ \mathrm{s}^{-1}$	Ta
k_{AB}	$30,000,000\ \mathrm{s}^{-1}$	Ta
k_{AU}	$333\ \mathrm{s}^{-1}$	Ta
k_{RyR}	$2 \cdot 10^8\ (\mathrm{Ms})^{-1}$	Ta

Initial receptor densities

Receptor	Density	Ref.
NMDAR	$150\ \mu\mathrm{m}^{-2}$	Be
AMPAR	$1200\ \mu\mathrm{m}^{-2}$	Be
VSCC	$2\ \mu\mathrm{m}^{-2}$	Be
PMCA	$998\ \mu\mathrm{m}^{-2}$	Be
NCX	$142\ \mu\mathrm{m}^{-2}$	Be
SERCA	$1000\ \mu\mathrm{m}^{-2}$	Be
b_f	$4791\ \mu\mathrm{m}^{-2}$	Be

Initial concentrations

Variable	Conc.	Ref.
$[Ca^{2+}]_{cyto}$	$1 \cdot 10^{-7}$ M	Ba
$[Ca^{2+}]_{SA}$	$150 \cdot 10^{-6}$ M	Doi
B_m	$2 \cdot 10^{-5}$ M	Be

VSCC receptors. VSCC dynamics are based on a five-state model proposed in Bartol et al. (2015) and Bell et al. (2022). The kinetic rate constants within these states are voltage-dependent. We use the same density assumption as in Bell et al. (2022) of 2 μm^{-2} based on measurements in apical dendrites (Magee and Johnston, 1995).

The VSCCs also allow for an influx of Ca^{2+} once they are open which is defined by the following equation:

$$\mathrm{VSCC} \xrightarrow{k_{\mathrm{VSCC}}} \mathrm{VSCC} + \mathrm{Ca}^{2+}_{\mathrm{cyto}} \ . \tag{5}$$

The rate $k_{\mathrm{VSCC}}(V_{\mathrm{m}}(\mathrm{t}))$ is membrane potential-dependent and given by the following expression:

$$k_{\mathrm{VSCC}}(V_{\mathrm{m}}(\mathrm{t})) = \frac{\gamma_{\mathrm{VSCC}} \cdot \mathrm{N_A}\left(0.393 - \exp\left(\frac{-V_{\mathrm{m}}(\mathrm{t})}{80.36}\right)\right)}{2 \cdot F\left(1 - \exp\left(\frac{-V_{\mathrm{m}}(\mathrm{t})}{80.36}\right)\right)} \ . \tag{6}$$

In addition, the reaction rate $a_{\mathrm{i}}(V_{\mathrm{m}}(\mathrm{t}))$ and $b_{\mathrm{i}}(V_{\mathrm{m}}(\mathrm{t}))$ describing the changes between VSCC states also depend on the transmembrane potential and are given by the

Table 3. Chemical reactions used in the model, with the exception of the RyR equations, which are listed in text. For clarity in the table, abbreviated reference labels are used: reactions marked DYK from De Young and Keizer (1992) and Si from Singh et al. (2021)

Reactions for IP_3Rs	Ref.
$IP_3R_{000} + IP_3 \underset{b_{1,IP3R}}{\overset{a_{1,IP3R}}{\rightleftharpoons}} IP_3R_{100}$	DYK
$IP_3R_{100} + Ca^{2+}_{cyto} \underset{b_{2,IP3R}}{\overset{a_{2,IP3R}}{\rightleftharpoons}} IP_3R_{101}$	DYK
$IP_3R_{001} + IP_3 \underset{b_{3,IP3R}}{\overset{a_{3,IP3R}}{\rightleftharpoons}} IP_3R_{101}$	DYK
$IP_3R_{000} + Ca^{2+}_{cyto} \underset{b_{4,IP3R}}{\overset{a_{4,IP3R}}{\rightleftharpoons}} IP_3R_{001}$	DYK
$IP_3R_{010} + IP_3 \underset{b_{1,IP3R}}{\overset{a_{1,IP3R}}{\rightleftharpoons}} IP_3R_{110}$	DYK
$IP_3R_{110} + Ca^{2+}_{cyto} \underset{b_{2,IP3R}}{\overset{a_{2,IP3R}}{\rightleftharpoons}} IP_3R_{111}$	DYK
$IP_3R_{011} + IP_3 \underset{b_{3,IP3R}}{\overset{a_{3,IP3R}}{\rightleftharpoons}} IP_3R_{111}$	DYK
$IP_3R_{010} + Ca^{2+}_{cyto} \underset{b_{4,IP3R}}{\overset{a_{4,IP3R}}{\rightleftharpoons}} IP_3R_{011}$	DYK
$IP_3R_{000} + Ca^{2+}_{cyto} \underset{b_{5,IP3R}}{\overset{a_{5,IP3R}}{\rightleftharpoons}} IP_3R_{010}$	DYK
$IP_3R_{100} + Ca^{2+}_{cyto} \underset{b_{5,IP3R}}{\overset{a_{5,IP3R}}{\rightleftharpoons}} IP_3R_{110}$	DYK
$IP_3R_{001} + Ca^{2+}_{cyto} \underset{b_{5,IP3R}}{\overset{a_{5,IP3R}}{\rightleftharpoons}} IP_3R_{011}$	DYK
$IP_3R_{101} + Ca^{2+}_{cyto} \underset{b_{5,IP3R}}{\overset{a_{5,IP3R}}{\rightleftharpoons}} IP_3R_{111}$	DYK
Reactions for mGlur and PLC	**Ref.**
$mGlur + glut. \underset{k_{mGlur,bGlu}}{\overset{k_{mGlur,fGlu}}{\rightleftharpoons}} mGlur.Glu$	Si
$mGlur.Glu \xrightarrow{k_{mGluR,Glu,IP3}} mGlur + glut. + IP_3$	Si
$glut. + mGlur.Glu \underset{k_{mGluR,Glu,bGlu}}{\overset{k_{mGluR,Glu,fGlu}}{\rightleftharpoons}} mGlur.Glu.Glu$	Si
$mGlur.Glu.Glu \xrightarrow{k_{mGluR,Glu,Glu,IP3}} mGlur.Glu + glut. + IP_3$	Si
$Ca^{2+}_{cyto} + PLC \underset{k_{PLC,bCa}}{\overset{k_{PLC,fCa}}{\rightleftharpoons}} PLC.Ca$	Si
$PLC.Ca \underset{k_{PLC,Ca,bPIP2}}{\overset{k_{PLC,Ca,fPIP2}}{\rightleftharpoons}} PLC.Ca.PIP2$	Si
$PLC.Ca.PIP2 \xrightarrow{k_{PLC,Ca,PIP2,IP3}} PLC.Ca + IP_3$	Si
$IP_3 \xrightarrow{k_{IP3,degrade}} \emptyset$	Si
$Ca^{2+}{}_{ER} + IP_3R_{110} \xrightarrow{k_{IP3R,Ca,flux}} Ca^{2+}_{cyto} + IP_3R_{110}$	Si

following expressions:

$$a_i(V_m(t)) = \alpha_i \cdot \exp\left(\frac{V_m(t)}{V_i}\right), \tag{7}$$

$$b_i(V_m(t)) = \beta_i \cdot \exp\left(\frac{V_m(t)}{V_i}\right). \tag{8}$$

Where α_i, β_i and V_i are specific parameters given in Table 2. The VSCCs were assumed to be homogeneously distributed in the spine plasma membrane.

PMCA, NCX and fixed buffers. For modelling PMCA, NCX and fixed buffers on the plasma membrane, the same equations and parameters as in Bartol et al. (2015) and Bell et al. (2022) were used. The PMCAs and NCXs were homogeneously distributed along the entire plasma membrane with a receptor density of 998 and 142 μm^{-2}, respectively. The fixed Ca^{2+} buffers were homogeneously distributed in the spine plasma membrane with a density of 4791 μm^{-2}.

Equations in the cytosol

We included two reactions occurring in the cytosol. These reactions are Ca^{2+} binding to mobile buffers as described in Schwaller (2010) and a decay term for Ca^{2+} to capture other Ca^{2+} buffering events in the cytosol. The decay parameter k_d was optimized using the ODE version of the model to match experimental data. See Section 4.4.

Receptors at the smooth ER membrane

In this section, we describe the receptor equations for RyRs and SERCA which are the receptors located at the smooth ER membrane. Our model only considers RyRs but not IP_3Rs based on Spacek and Harris (1997), where they showed that RyRs are more common in dendritic spines while IP_3Rs in the dendritic shaft.

RyR. **RyR dynamics**. The presence of RyRs in neurons is well known (Ellisman et al., 1990; McPherson & Campbell, 1993; McPhersonx et al., 1991; Sharp et al., 1993; Walton et al., 1991). However, to the authors' knowledge, there is no existing mathematical model that has been specifically designed to match neural RyR experimental data. Therefore, to simulate the effects of RyRs in dendritic spines, we used the cardiac model formulated by Tanskanen et al. (2007). Their model adaptations allow us to use the four-state model (closed RyR_C, open RyR_O, closed inactivated RyR_{CI} and open-inactivated RyR_{OI}) from Stern et al. (1999) and Wang et al. (2004) in particle-based modelling. It is additionally assumed that each RyR contains four Ca^{2+} binding activating sites (RyR(a)) and four Ca^{2+} binding inactivating sites (RyR(i)). Thus each of the original four states has different possible sub-states depending on the number of Ca^{2+} ions bound to the activating and inactivating sites $RyR_{j_s}(a \sim j_a, i \sim j_i)$ with $j_s = \{C, O, CI, OI\}$ representing the four states, $j_a = \{0, 1, 2, 3, 4\}$ representing the number of Ca^{2+} molecules bound to the activating sites, and $j_i = \{0, 1, 2, 3, 4\}$ representing the number of Ca^{2+} molecules bound to the inactivating sites. Therefore, counting states and sub-states (the sub-states are given by the number of Ca^{2+} ions bound to the different sites), the modified model contains 100 possible states, instead of four. The following reactions represent cytosolic Ca^{2+} binding to the activating sites of the RyRs, independently of how many molecules are bound to the inactivating sites. The reaction rate constants are given in Table 2.

$$\mathrm{RyR}_{\mathrm{C}}(0,\ j_{\mathrm{i}}) + \mathrm{Ca}^{2+}_{\mathrm{cyto}} \xrightleftharpoons[1\mathrm{k}_{\mathrm{k}_{\mathrm{AU}}}]{4\mathrm{k}_{\mathrm{k}_{\mathrm{AB}}}} \mathrm{RyR}_{\mathrm{C}}(1,\ j_{\mathrm{i}})\ ,$$

$$\mathrm{RyR}_{\mathrm{C}}(1,\ j_{\mathrm{i}}) + \mathrm{Ca}^{2+}_{\mathrm{cyto}} \xrightleftharpoons[2\mathrm{k}_{\mathrm{AU}}]{3\mathrm{k}_{\mathrm{AB}}} \mathrm{RyR}_{\mathrm{C}}(2,\ j_{\mathrm{i}})\ ,$$

$$\mathrm{RyR}_{\mathrm{C}}(2,\ j_{\mathrm{i}}) + \mathrm{Ca}^{2+}_{\mathrm{cyto}} \xrightleftharpoons[3\mathrm{k}_{\mathrm{AU}}]{2\mathrm{k}_{\mathrm{AB}}} \mathrm{RyR}_{\mathrm{C}}(3,\ j_{\mathrm{i}})\ ,$$

$$\mathrm{RyR}_{\mathrm{C}}(3,\ j_{\mathrm{i}}) + \mathrm{Ca}^{2+}_{\mathrm{cyto}} \xrightleftharpoons[4\mathrm{k}_{\mathrm{AU}}]{1\mathrm{k}_{\mathrm{AB}}} \mathrm{RyR}_{\mathrm{C}}(4,\ j_{\mathrm{i}})\ ,$$

$$\mathrm{RyR}_{\mathrm{CI}}(0,\ j_{\mathrm{i}}) + \mathrm{Ca}^{2+}_{\mathrm{cyto}} \xrightleftharpoons[1\mathrm{k}_{\mathrm{AU}}]{4\mathrm{k}_{\mathrm{AB}}} \mathrm{RyR}_{\mathrm{CI}}(1,\ j_{\mathrm{i}})\ ,$$

$$\mathrm{RyR}_{\mathrm{CI}}(1,\ j_{\mathrm{i}}) + \mathrm{Ca}^{2+}_{\mathrm{cyto}} \xrightleftharpoons[2\mathrm{k}_{\mathrm{AU}}]{3\mathrm{k}_{\mathrm{AB}}} \mathrm{RyR}_{\mathrm{CI}}(2,\ j_{\mathrm{i}})\ ,$$

$$\mathrm{RyR}_{\mathrm{CI}}(2,\ j_{\mathrm{i}}) + \mathrm{Ca}^{2+}_{\mathrm{cyto}} \xrightleftharpoons[3\mathrm{k}_{\mathrm{AU}}]{2\mathrm{k}_{\mathrm{AB}}} \mathrm{RyR}_{\mathrm{CI}}(3,\ j_{\mathrm{i}})\ ,$$

$$\mathrm{RyR}_{\mathrm{CI}}(3,\ j_{\mathrm{i}}) + \mathrm{Ca}^{2+}_{\mathrm{cyto}} \xrightleftharpoons[4\mathrm{k}_{\mathrm{AU}}]{1\mathrm{k}_{\mathrm{AB}}} \mathrm{RyR}_{\mathrm{CI}}(4,\ j_{\mathrm{i}})\ ,$$

$$\mathrm{RyR}_{\mathrm{O}}(0,\ j_{\mathrm{i}}) + \mathrm{Ca}^{2+}_{\mathrm{cyto}} \xrightleftharpoons[1\mathrm{k}_{\mathrm{AU}}]{4\mathrm{k}_{\mathrm{AB}}} \mathrm{RyR}_{\mathrm{O}}(1,\ j_{\mathrm{i}})\ ,$$

$$\mathrm{RyR}_{\mathrm{O}}(1,\ j_{\mathrm{i}}) + \mathrm{Ca}^{2+}_{\mathrm{cyto}} \xrightleftharpoons[2\mathrm{k}_{\mathrm{AU}}]{3\mathrm{k}_{\mathrm{AB}}} \mathrm{RyR}_{\mathrm{O}}(2,\ j_{\mathrm{i}})\ ,$$

$$\mathrm{RyR}_{\mathrm{O}}(2,\ j_{\mathrm{i}}) + \mathrm{Ca}^{2+}_{\mathrm{cyto}} \xrightleftharpoons[3\mathrm{k}_{\mathrm{AU}}]{2\mathrm{k}_{\mathrm{AB}}} \mathrm{RyR}_{\mathrm{O}}(3,\ j_{\mathrm{i}})\ ,$$

$$\mathrm{RyR}_{\mathrm{O}}(3,\ j_{\mathrm{i}}) + \mathrm{Ca}^{2+}_{\mathrm{cyto}} \xrightleftharpoons[4\mathrm{k}_{\mathrm{AU}}]{1\mathrm{k}_{\mathrm{AB}}} \mathrm{RyR}_{\mathrm{O}}(4,\ j_{\mathrm{i}})\ ,$$

$$\mathrm{RyR}_{\mathrm{OI}}(0,\ j_{\mathrm{i}}) + \mathrm{Ca}^{2+}_{\mathrm{cyto}} \xrightleftharpoons[1\mathrm{k}_{\mathrm{AU}}]{4\mathrm{k}_{\mathrm{AB}}} \mathrm{RyR}_{\mathrm{OI}}(1,\ j_{\mathrm{i}})\ ,$$

$$\mathrm{RyR}_{\mathrm{OI}}(1,\ j_{\mathrm{i}}) + \mathrm{Ca}^{2+}_{\mathrm{cyto}} \xrightleftharpoons[2\mathrm{k}_{\mathrm{AU}}]{3\mathrm{k}_{\mathrm{AB}}} \mathrm{RyR}_{\mathrm{OI}}(2,\ j_{\mathrm{i}})\ ,$$

$$\mathrm{RyR}_{\mathrm{OI}}(2,\ j_{\mathrm{i}}) + \mathrm{Ca}^{2+}_{\mathrm{cyto}} \xrightleftharpoons[3\mathrm{k}_{\mathrm{AU}}]{2\mathrm{k}_{\mathrm{AB}}} \mathrm{RyR}_{\mathrm{OI}}(3,\ j_{\mathrm{i}})\ ,$$

$$\mathrm{RyR}_{\mathrm{OI}}(3,\ j_{\mathrm{i}}) + \mathrm{Ca}^{2+}_{\mathrm{cyto}} \xrightleftharpoons[4\mathrm{k}_{\mathrm{AU}}]{1\mathrm{k}_{\mathrm{AB}}} \mathrm{RyR}_{\mathrm{OI}}(4,\ j_{\mathrm{i}})\ . \tag{9}$$

The following reactions represent cytosolic Ca^{2+} binding to the inactivating sites of the RyRs, independently of how many molecules are bound to the activating sites. Note that the binding rates for cytosolic Ca^{2+} binding to the closed states (k_{IC}) are different from those for cytosolic Ca^{2+} binding to the open states (k_{IO}).

$$\mathrm{RyR}_{\mathrm{C}}(j_{\mathrm{a}},\ 0) + \mathrm{Ca}^{2+}_{\mathrm{cyto}} \xrightleftharpoons[1\mathrm{k}_{\mathrm{IU}}]{4\mathrm{k}_{\mathrm{IC}}} \mathrm{RyR}_{\mathrm{C}}(j_{\mathrm{a}},\ 1)\ ,$$

$$\mathrm{RyR}_{\mathrm{C}}(j_{\mathrm{a}},\ 1) + \mathrm{Ca}^{2+}_{\mathrm{cyto}} \xrightleftharpoons[2\mathrm{k}_{\mathrm{IU}}]{3\mathrm{k}_{\mathrm{IC}}} \mathrm{RyR}_{\mathrm{C}}(j_{\mathrm{a}},\ 2)\ ,$$

$$\mathrm{RyR}_{\mathrm{C}}(j_{\mathrm{a}},\ 2) + \mathrm{Ca}^{2+}_{\mathrm{cyto}} \xrightleftharpoons[3\mathrm{k}_{\mathrm{IU}}]{2\mathrm{k}_{\mathrm{IC}}} \mathrm{RyR}_{\mathrm{C}}(j_{\mathrm{a}},\ 3)\ ,$$

$$\mathrm{RyR}_{\mathrm{C}}(j_{\mathrm{a}},\ 3) + \mathrm{Ca}^{2+}_{\mathrm{cyto}} \xrightleftharpoons[4\mathrm{k}_{\mathrm{IU}}]{1\mathrm{k}_{\mathrm{IC}}} \mathrm{RyR}_{\mathrm{C}}(j_{\mathrm{a}},\ 4)\ ,$$

$$\mathrm{RyR}_{\mathrm{CI}}(j_{\mathrm{a}},\ 0) + \mathrm{Ca}^{2+}_{\mathrm{cyto}} \xrightleftharpoons[1\mathrm{k}_{\mathrm{IU}}]{4\mathrm{k}_{\mathrm{IC}}} \mathrm{RyR}_{\mathrm{CI}}(j_{\mathrm{a}},\ 1)\ ,$$

$$\mathrm{RyR}_{\mathrm{CI}}(j_{\mathrm{a}},\ 1) + \mathrm{Ca}^{2+}_{\mathrm{cyto}} \xrightleftharpoons[2\mathrm{k}_{\mathrm{IU}}]{3\mathrm{k}_{\mathrm{IC}}} \mathrm{RyR}_{\mathrm{CI}}(j_{\mathrm{a}},\ 2)\ ,$$

$$\mathrm{RyR}_{\mathrm{CI}}(j_{\mathrm{a}},\ 2) + \mathrm{Ca}^{2+}_{\mathrm{cyto}} \xrightleftharpoons[3\mathrm{k}_{\mathrm{IU}}]{2\mathrm{k}_{\mathrm{IC}}} \mathrm{RyR}_{\mathrm{CI}}(j_{\mathrm{a}},\ 3)\ ,$$

$$\mathrm{RyR}_{\mathrm{CI}}(j_{\mathrm{a}},\ 3) + \mathrm{Ca}^{2+}_{\mathrm{cyto}} \xrightleftharpoons[4\mathrm{k}_{\mathrm{IU}}]{1\mathrm{k}_{\mathrm{IC}}} \mathrm{RyR}_{\mathrm{CI}}(j_{\mathrm{a}},\ 4)\ ,$$

$$\mathrm{RyR}_{\mathrm{O}}(j_{\mathrm{a}},\ 0) + \mathrm{Ca}^{2+}_{\mathrm{cyto}} \xrightleftharpoons[1\mathrm{k}_{\mathrm{IU}}]{4\mathrm{k}_{\mathrm{IO}}} \mathrm{RyR}_{\mathrm{O}}(j_{\mathrm{a}},\ 1)\ ,$$

$$\mathrm{RyR}_{\mathrm{O}}(j_{\mathrm{a}},\ 1) + \mathrm{Ca}^{2+}_{\mathrm{cyto}} \xrightleftharpoons[2\mathrm{k}_{\mathrm{IU}}]{3\mathrm{k}_{\mathrm{IO}}} \mathrm{RyR}_{\mathrm{O}}(j_{\mathrm{a}},\ 2)\ ,$$

$$\mathrm{RyR}_{\mathrm{O}}(j_{\mathrm{a}},\ 2) + \mathrm{Ca}^{2+}_{\mathrm{cyto}} \xrightleftharpoons[3\mathrm{k}_{\mathrm{IU}}]{2\mathrm{k}_{\mathrm{IO}}} \mathrm{RyR}_{\mathrm{O}}(j_{\mathrm{a}},\ 3)\ ,$$

$$\mathrm{RyR}_{\mathrm{O}}(j_{\mathrm{a}},\ 3) + \mathrm{Ca}^{2+}_{\mathrm{cyto}} \xrightleftharpoons[4\mathrm{k}_{\mathrm{IU}}]{1\mathrm{k}_{\mathrm{IO}}} \mathrm{RyR}_{\mathrm{O}}(j_{\mathrm{a}},\ 4)\ ,$$

$$\mathrm{RyR}_{\mathrm{OI}}(j_{\mathrm{a}},\ 0) + \mathrm{Ca}^{2+}_{\mathrm{cyto}} \xrightleftharpoons[1\mathrm{k}_{\mathrm{IU}}]{4\mathrm{k}_{\mathrm{IO}}} \mathrm{RyR}_{\mathrm{OI}}(j_{\mathrm{a}},\ 1)\ ,$$

$$\mathrm{RyR}_{\mathrm{OI}}(j_{\mathrm{a}},\ 1) + \mathrm{Ca}^{2+}_{\mathrm{cyto}} \xrightleftharpoons[2\mathrm{k}_{\mathrm{IU}}]{3\mathrm{k}_{\mathrm{IO}}} \mathrm{RyR}_{\mathrm{OI}}(j_{\mathrm{a}},\ 2)\ ,$$

$$\mathrm{RyR}_{\mathrm{OI}}(j_{\mathrm{a}},\ 2) + \mathrm{Ca}^{2+}_{\mathrm{cyto}} \xrightleftharpoons[3\mathrm{k}_{\mathrm{IU}}]{2\mathrm{k}_{\mathrm{IO}}} \mathrm{RyR}_{\mathrm{OI}}(j_{\mathrm{a}},\ 3)\ ,$$

$$\mathrm{RyR}_{\mathrm{OI}}(j_{\mathrm{a}},\ 3) + \mathrm{Ca}^{2+}_{\mathrm{cyto}} \xrightleftharpoons[4\mathrm{k}_{\mathrm{IU}}]{1\mathrm{k}_{\mathrm{IO}}} \mathrm{RyR}_{\mathrm{OI}}(j_{\mathrm{a}},\ 4)\ . \tag{10}$$

The following reactions represent the transition between closed and open RyRs. The RyRs are always able to close with rate β, independently on how many cytosolic Ca^{2+} molecules are bound to the activating or inactivating sites. However, for the RyRs to open, at least four activation sites must be bound to cytosolic Ca^{2+}.

$$\begin{aligned}
&\mathrm{RyR_C}(0,\ j_\mathrm{i}) \xleftarrow{\beta} \mathrm{RyR_O}(0,\ j_\mathrm{i})\ ,\\
&\mathrm{RyR_C}(1,\ j_\mathrm{i}) \xleftarrow{\beta} \mathrm{RyR_O}(1,\ j_\mathrm{i})\ ,\\
&\mathrm{RyR_C}(2,\ j_\mathrm{i}) \xleftarrow{\beta} \mathrm{RyR_O}(2,\ j_\mathrm{i})\ ,\\
&\mathrm{RyR_C}(3,\ j_\mathrm{i}) \xleftarrow{\beta} \mathrm{RyR_O}(3,\ j_\mathrm{i})\ ,\\
&\mathrm{RyR_C}(4,\ j_\mathrm{i}) \xrightleftharpoons[\beta]{\alpha} \mathrm{RyR_O}(4,\ j_\mathrm{i})\ .
\end{aligned} \tag{11}$$

The following reaction governs the transition between closed inactivated and open inactivated RyRs, which occurs independently of the number of cytosolic Ca^{2+} molecules bound to the activating and inactivating sites.

$$\mathrm{RyR_{CI}} \xrightleftharpoons[\beta]{\alpha} \mathrm{RyR_{OI}}\ . \tag{12}$$

The following reactions represent the transition between closed and closed-inactivated RyRs.

$$\begin{aligned}
&\mathrm{RyR_C}(j_\mathrm{a},\ 0) \xleftarrow{\gamma} \mathrm{RyR_{CI}}(j_\mathrm{a},\ 0)\ ,\\
&\mathrm{RyR_C}(j_\mathrm{a},\ 1) \xrightleftharpoons[\gamma]{\delta'} \mathrm{RyR_{CI}}(j_\mathrm{a},\ 1)\ ,\\
&\mathrm{RyR_C}(j_\mathrm{a},\ 2) \xrightleftharpoons[\gamma]{\delta'} \mathrm{RyR_{CI}}(j_\mathrm{a},\ 1)\ ,\\
&\mathrm{RyR_C}(j_\mathrm{a},\ 3) \xrightleftharpoons[\gamma]{\delta'} \mathrm{RyR_{CI}}(j_\mathrm{a},\ 3)\ ,\\
&\mathrm{RyR_C}(j_\mathrm{a},\ 4) \xrightleftharpoons[\gamma]{\delta'} \mathrm{RyR_{CI}}(j_\mathrm{a},\ 4)\ .
\end{aligned} \tag{13}$$

The inactivation rate δ' is non-zero if at least one Ca^{2+} molecule is bound to an inactivation site. The following reactions represent the transition between open and open-inactivated RyRs.

$$\begin{aligned}
&\mathrm{RyR_O}(j_\mathrm{a},\ 0) \xleftarrow{\gamma} \mathrm{RyR_{OI}}(j_\mathrm{a},\ 0)\ ,\\
&\mathrm{RyR_O}(j_\mathrm{a},\ 1) \xrightleftharpoons[\gamma]{\delta} \mathrm{RyR_{OI}}(j_\mathrm{a},\ 1)\ ,\\
&\mathrm{RyR_O}(j_\mathrm{a},\ 2) \xrightleftharpoons[\gamma]{\delta} \mathrm{RyR_{OI}}(j_\mathrm{a},\ 2)\ ,\\
&\mathrm{RyR_O}(j_\mathrm{a},\ 3) \xrightleftharpoons[\gamma]{\delta} \mathrm{RyR_{OI}}(j_\mathrm{a},\ 3)\ ,\\
&\mathrm{RyR_O}(j_\mathrm{a},\ 4) \xrightleftharpoons[\gamma]{\delta} \mathrm{RyR_{OI}}(j_\mathrm{a},\ 4)\ .
\end{aligned} \tag{14}$$

The inactivation rate δ is non-zero if at least one cytosolic Ca^{2+} molecule is bound to the inactivation site.

RyR flux rate. Once the RyRs are opened, Ca^{2+} can efflux from the ER to the cytosol due to the Ca^{2+} concentration gradient. However we assume a bidirectional reaction as a small influx from the cytosol into the ER is technically also possible. The reaction describing the flux of Ca^{2+} is given by the following expression:

$$[\mathrm{Ca^{2+}}]_\mathrm{ER} + \mathrm{RyR_O} \xrightleftharpoons[k_\mathrm{RyR}]{k_\mathrm{RyR}} [\mathrm{Ca^{2+}}]_\mathrm{cyt} + \mathrm{RyR_O}\ . \tag{15}$$

The RyR reaction rate constant k_{RyR} was set to a value of $1.09 \times 10^9\ \mathrm{M^{-1}s^{-1}}$ as suggested by Singh et al. (2021).

RyR density. We could not find any direct measurements of RyR density in dendritic spines. However this has been studied in cardiomyocytes using super-resolution imaging (Hou et al., 2021; Kolstad et al., 2018; Shen et al., 2019). Shen et al. (2019) measured around 3.4 Ca^{2+} release units per μm^3 in rat cardiomyocytes, with a Ca^{2+} release unit containing around 20–25 RyRs. Furthermore, Hou et al. (2021) measured a Ca^{2+} release unit density of around 1.1 per μm^2. To keep our RyR within a similar range to these measured values in the homogeneous cases of both ER geometries, we chose to place 60 RyRs and keep this number constant for all distributions. In our simulations RyRs were modelled as functioning individually, with each RyR represented as an independent reactive site within the spatial geometry. This approach allows us to capture stochastic effects, where the opening and closing of each RyR are treated as probabilistic events, governed by local calcium concentrations. Although RyRs are modelled as independent entities, they act in a coupled manner through CICR. This coupling arises naturally in MCell simulations, as the calcium released by one RyR diffuses locally and can activate neighbouring RyRs. The emergent dynamics of CICR, including wave propagation or local clustering of RyR activity, are thus captured without the need for explicit coupling mechanisms. This allows us to explore how spatial distributions of RyRs influence cooperative behaviour and calcium signalling at a systems level.

SERCA. We employ the same SERCA pump model as in Bell et al. (2022), which was originally formulated in Bartol et al. (2015). The SERCA density at the membrane is $1000\ \mu m^{-2}$ (Bartol et al., 2015). We estimated the SERCA

Table 4. Reaction rates and parameters used for the simulation. For clarity in the table, abbreviated reference labels are used: reactions marked DYK from De Young and Keizer (1992), OG from Ornelas-Guevara et al. (2023), Kim from Kim et al. (2013), Me from Means et al. (2006) and Si from Singh et al. (2021)

Parameters for IP_3Rs

Name	Value	Ref.
$a_{1,IP3R}$	$4 \cdot 10^8\ (Ms)^{-1}$	DYK
$a_{2,IP3R}$	$2 \cdot 10^5\ (Ms)^{-1}$	DYK
$a_{3,IP3R}$	$4 \cdot 10^8\ (Ms)^{-1}$	DYK
$a_{4,IP3R}$	$2 \cdot 10^5\ (Ms)^{-1}$	DYK
$a_{5,IP3R}$	$2 \cdot 10^7\ (Ms)^{-1}$	DYK
$b_{1,IP3R}$	$52\ s^{-1}$	DYK
$b_{2,IP3R}$	$0.21\ s^{-1}$	DYK
$b_{3,IP3R}$	$377.36\ s^{-1}$	DYK
$b_{4,IP3R}$	$0.0289\ s^{-1}$	DYK
$a_{5,IP3R}$	$1.6468\ s^{-1}$	DYK

Initial concentrations

Name	Value	Ref.
IP_3	$50 \cdot 10^{-9}$ M	OG
mGlur	$602.2\ \mu m^{-2}$	Kim
PLC	$120.44\ \mu m^{-2}$	Kim
IP_3R_{000}	$26.389\ \mu m^{-2}$	Me

Parameters for mGlur

Name	Value	Ref.
$k_{mGluR,fGlu}$	$1 \cdot 10^8\ (Ms)^{-1}$	Si
$k_{mGluR,bGlu}$	$7.85\ s^{-1}$	Si
$k_{mGluR,Glu,IP3}$	$0.03875\ s^{-1}$	Si
$k_{mGluR,Glu,fGlu}$	$2 \cdot 10^6\ (Ms)^{-1}$	Si
$k_{mGluR,Glu,bGlu}$	$15.7\ s^{-1}$	Si
$k_{mGluR,Glu,Glu,IP3R}$	$0.0775\ s^{-1}$	Si
$k_{PLC,fCa}$	$3 \cdot 10^6\ (Ms)^{-1}$	Si
$k_{PLC,bCa}$	$1\ s^{-1}$	Si
$k_{PLC,Ca,fPIP2}$	$25\ s^{-1}$	Si
$k_{PLC,Ca,bPIP2}$	$10\ s^{-1}$	Si
$k_{PLC,Ca,PIP2,IP3}$	$0.155\ s^{-1}$	Si
$k_{IP3,degrade}$	$0.28\ s^{-1}$	Si
$k_{IP3R,Ca,flux}$	$1.19 \cdot 10^8\ (Ms)^{-1}$	Si

Ca^{2+} leak parameter by optimizing the ODE curve to match the experimental data from Segal and Korkotian (2014).

IP_3R. The equations and parameters for modelling the IP_3Rs are given in Tables 3 and 4, respectively. The IP_3R model from De Young and Keizer (1992) was used combined with the mGLur and PLC equations from Singh et al. (2021).

Table 5. Surface area, volume and surface area to volume ratio (SA/*V*) for the different plasma membranes and ERs used

	Idealized PM		Realistic PM	
	Plasma membrane		Plasma membrane	
Surface area	$7.18\ \mu m^2$		$6.63\ \mu m^2$	
Volume	$1.05\ \mu m^3$		$0.67\ \mu m^3$	
Ratio SA/V	$6.83/\mu m$		$9.88/\mu m$	
	Idealized ER	Laminar SA	Idealized ER	Laminar SA
Surface area	$1.28\ \mu m^2$	$2.20\ \mu m^2$	$1.24\ \mu m^2$	$2.40\ \mu m^2$
Volume	$0.052\ \mu m^3$	$0.049\ \mu m^3$	$0.027\ \mu m^3$	$0.027\ \mu m^3$
Ratio SA/V	$24.47/\mu m$	$44.74/\mu m$	$45.8/\mu m$	$88.47/\mu m$

ODE model

To optimize the parameters k_d and $k_{S,leak}$, which represent the Ca^{2+} decay and SERCA leak terms, respectively, we developed a compartmental ODE version of the model. We used VCell (Resasco et al., 2012) to formulate the initial flux equations between compartments and ran the model in MATLAB using the ode solver `ode15s`. The model was first developed without an SA compartment to confirm that the ODE model matched the spatial simulations with no ER as described by Bell et al. (2022). Next, an inactive ER compartment, including SERCA but no RyRs, was added to the ODE model, which was used to replicate the corresponding MCell simulations. Lastly RyRs were included in the ER compartment of the ODE model. As described in Section 4.3.1, the RyR model we considered contains 100 states. A model with 100 states would be very complex to be implemented in an ODE model. However, this model is a detailed expansion of a four-state model originally formulated by Stern et al. (1999) and Wang et al. (2004) which allows for particle-based simulations. Therefore we implemented the four-state model within the ODE framework and reliably replicated the dynamics obtained using the spatial stochastic particle-based simulations. This ODE model was then used to calculate the parameters k_d and $k_{S,leak}$ by fitting them to experimental data from Segal and Korkotian (2014) using the MATLAB function for solving non-linear least squares problems.

Stimulus and further simulation details

We use the same stimulus approach as in Bell et al. (2022) and Bartol et al. (2015), which consists of a plasma membrane depolarization and glutamate release, which subsequently diffuses within the synaptic cleft and activates the NMDARs (Fig. 1). The plasma membrane depolarization includes an excitatory postsynaptic potential (ESPS) and a back propagating action potential (BPAP). The glutamate molecules are released instantaneously at the geometrical centre of the PSD. We also tested a simulation set-up including only an ESPS and realized that no RyRs opened using this set-up. This outcome suggests that the EPSP alone is insufficient to trigger calcium-induced calcium release (CICR) via RyRs, highlighting the importance of the combined stimulus (local EPSP followed by global bAP) for robust CICR activation.

A further point of discussion is the SERCA distribution. Basnayake et al. (2019) measured SERCA to be mostly located at the synaptopodin sites, which correspond with the sites with highest laminarity. However, by increasing the surface area towards the upper part of the SA and keeping the SERCA density constant, we ensured that a higher number of SERCA were located there.

An initial Ca^{2+} concentration of 100 nM is assumed in the cytosol before the stimulus. After glutamate release, Ca^{2+} is released through NMDARs (in the PSD) and VSCCs (in the plasma membrane) due to glutamatergic simulation in the centre of the PSD and plasma membrane depolarization. Through the mechanism known as Ca^{2+}-induced Ca^{2+} release, further Ca^{2+} ions are then released from the RyRs. At the longitudinal ends of the dendrite, reflective boundary conditions were assumed.

For each simulation set-up, we ran 250 realizations in MCell4 (Husar et al., 2022) and calculated mean number of Ca^{2+} ions and standard error of the mean. The Ca^{2+} transient plots are generated using `stdshade` (Musall, 2023) in Matlab version 2022a. In RyR distributions and geometries with fewer than 50 opened RyRs, we ran 150 or so further simulations.

Geometries

To study the effects of the SA on Ca^{2+} handling, we utilized idealized and realistic geometries of both the plasma membrane and the ER. Figure 1*C* depicts the four geometries used in this work, which are a combination of idealized and realistic plasma membrane and non-laminar SER and laminar SA.

For the idealized plasma membrane geometry, we used the mushroom-shaped spine geometry from Bell et al. (2022) and Alimohamadi et al. (2021). We expanded this original idealized geometry to include a piece of dendrite to calculate how much Ca^{2+} reaches the dendrite in different conditions. The included dendrite consists of a cylindrical structure with a diameter of 1 μm as described in Benavides-Piccione et al. (2020) and a length of 1 μm (see Fig. 2). The ratio between SA diameter in the dendrite to dendrite diameter was set to 0.166 μm as described in Leung et al. (2021). A comparison between simulations including a piece of dendrite and the simulations from Bell et al. (2022) is given in Fig. 2*E*. For the ER geometries used in the geometries with idealized plasma membranes, we also differentiated between non-laminar SER and laminar SA. For the non-laminar case we used the same approach as in Bell et al. (2019) and Bell et al. (2022) by considering a ‘spine within a spine’. However the shape of the mature SA is characterized by its laminar structure consisting of stacked ER cisternae (Konietzny et al., 2022). Thus we also designed an idealized SA with laminar stacked discs.

For the realistic spine geometry, we use the plasma membrane and SA segmented and meshed by Lee et al. (2020), originally imaged by Wu et al. (2017) using focused ion beam scanning electron microscopy in the mouse cerebral cortex. The realistic SA from Lee et al. (2020) demonstrates the characteristic laminar shape. The realistic plasma membrane geometry includes two PSDs in contrast to the single PSD of the idealized geometry Fig. 5*A*. For both the idealized and the realistic plasma membrane, glutamate was released at the centre of the single PSDs at the beginning of the simulation, and the values are given in Table 6. To systematically study the effect of laminar SA structures, we additionally included an idealized non-laminar ER geometry for the realistic plasma membrane by removing the laminarity and smoothing the ER. The laminar structure of an SA results in a much higher surface area to volume ratio in the ER head. The differences in surface area, volume and surface area to volume ratio of all SAs are given in Table 5.

Table 6. Number of NMDAR, AMPAR and glutamate used for the idealized and realistic plasma membrane simulations. The density of the receptors and the ratio of glutamate to receptors are kept constant in both plasma membrane geometries

	Idealized PM	Realistic PM	
		Site 1	Site 2
Surface area of PSD	0.21 μm^2	0.15 μm^2	0.18 μm^2
Number of NMDAR	35	26	30
Number of AMPAR	278	204	237
Number of glutamate	500	367	426

Additional equations for including store-operated Ca^{2+} entry in the ODE model

In this section, we expand our ODE version of the model to include store-operated Ca^{2+} entry (SOCE). To do so we included the equations from Saftenku (2022). As described in Saftenku (2022), the probability of SOCE activation was given by the following equations:

$$P^{\infty}_{\rm SOCE} = \frac{K^4_{\rm d,SOCE}}{K^4_{\rm d,SOCE} + [{\rm Ca}^{2+}]^4_{\rm ER}}\,, \tag{16}$$

$$\frac{{\rm dP}_{\rm SOCE}}{\rm dt} = \frac{P^{\infty}_{\rm SOCE} - {\rm P}_{\rm SOCE}}{\tau_{\rm SOCE}}\,, \tag{17}$$

where $K^4_{\rm d,SOCE} = 75\ \mu{\rm M}$ is the dissociation constant, $\tau_{\rm SOCE} = 10$ s is the time constant of SOCE activation and ${\rm P}_{\rm SOCE}$ is the probability of SOCE activation. The change in $[{\rm Ca}^{2+}]_{\rm cyto}$ resulting from SOCE is described by the following rate:

$${\rm R}_{\rm SOCE} = k_{\rm SOCE}[{\rm Ca}^{2+}]_{\rm e}{\rm P}_{\rm SOCE} \tag{18}$$

where $k_{\rm SOCE} = 0.0222$ s and $[{\rm Ca}^{2+}]_{\rm e}$ is the extracellular Ca^{2+} concentration which we set to 2 mM. All parameters were taken from Saftenku (2022). We observed that including the SOCE model had almost no impact in the Ca^{2+} concentration. This matches with the experimental observations that Orai1 induces Ca^{2+} signals in the order of several seconds (Schober et al., 2019; Lis et al., 2007; Mercer et al., 2006), whereas our simulations are of 35 ms.

Use of Generative AI Tools

In the preparation of this manuscript, we used a generative artificial intelligence (GAI) tool – OpenAI's ChatGPT (model GPT-4, accessed via chat.openai.com) for language revision purposes only. This included assistance with improving grammar, clarity and readability of the text. The tool was not used for data analysis, figure generation or conceptual content creation. All content generated by the GAI tool was carefully reviewed, edited and verified by the authors to ensure accuracy and compliance with scientific standards. The authors take full responsibility for the integrity and accuracy of all aspects of the manuscript.

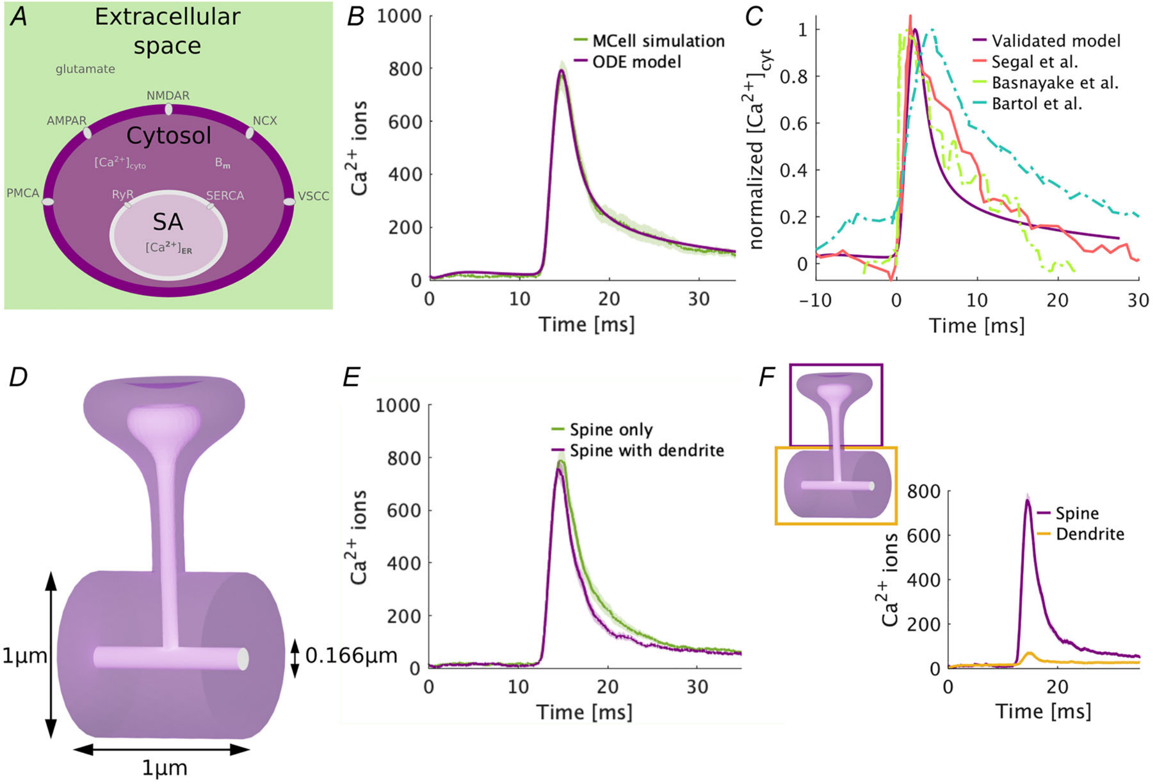

Figure 2. Model calibration

(A) Schematic of the compartmental ODE model used for the parameter estimation. (B) Comparison between the ODE model and the MCell simulations, assuming a homogeneous distribution of the RyRs. (C) ODE model optimized to fit the experimental data from Segal and Korkotian (2014). Our data are compared to further experimental measurements (Basnayake et al., 2019) and to other computational models (Bartol et al., 2015). (D) Spine with dendrite used for the ideal case simulations. The mushroom shape spine was extended with a cylinder to simulate the dendrite. (E) Comparison of the MCell simulations between using only a mushroom shaped spine and using the geometry in (A). Mean and standard error of the mean are shown. (F) Throughout the paper, the results will show Ca^{2+} transients at the spine and dendrite. Panel (F) depicts the geometric compartments used to delineate these measurements.

Results

To understand the relationship between spine geometry, ER geometry and RyR localization, we used both idealized and realistic geometries from the literature (Alimohamadi et al., 2021; Lee et al., 2020) in a spatial, particle-based stochastic model implemented in MCell4 (Husar et al., 2022) and stimulated NMDAR and VSCC activation by including both membrane depolarization and glutamate release. Our simulations reveal the following relationships: RyR opening probability is location-dependent and spine-geometry-dependent. Importantly mobile and immobile Ca^{2+} buffers and SERCA can provide some buffering against runaway potentiation of spines even when CICR is activated. The shape of the synapse affects NMDAR opening probability. For higher Ca^{2+} levels in spine heads, non-laminar SER and high NMDAR opening with RyR localized at the head are favourable. For higher Ca^{2+} levels in the dendrite, with a potential for spine-to-spine communication, laminar SA, neck localization of RyR and dendritic localization of IP_3Rs is favourable. We elaborate on these findings below.

RyR distribution affects opening probability and Ca^{2+} dynamics in an idealized, non-laminar SER

To study the effect of different spatial distributions of the RyRs within the SA, we first assumed a smooth, idealized geometry for both the plasma membrane and non-laminar SER (Fig. 1*C.i*). We investigated Ca^{2+} dynamics for four different RyR distributions in this geometry: a homogeneous distribution throughout the whole SER section (Homog. set-up), RyRs concentrated at the uppermost part of the SA close to the PSD (head set-up), RyRs concentrated in the spine neck but completely within the spine volume (neck set-up) and RyRs concentrated in the lowest part of the SA which overlaps both the spine and dendrite volumes (low neck set-up) (Fig. 3*A*). In all cases, the total number of RyRs was held constant (60 RyRs) and we conducted $|\mathbf{N}| = 250$ simulations for each scenario. To ensure consistency, the area over which RyRs were distributed was maintained at 0.07 μm^2 for the head, neck and low neck set-up. This approach ensured uniform RyR densities across these configurations, allowing us to isolate the effects of RyR localization and geometry on Ca^{2+} dynamics. For the homogeneous set-up, however, RyRs were distributed across the entire SA, resulting in a different density. As we and others have shown before (Hernández Mesa et al., 2022; Kolstad et al., 2018), due to the stochastic nature of the model, RyRs open only in a subset of those simulations $\mathbf{n} \in \mathbf{N}$. Thus the remaining set $\mathbf{N}\backslash\mathbf{n}$ is the set of simulations where RyRs did not open.

We observed that the location of the RyRs significantly impacts the probability of RyR opening during a given simulation (Fig. 3*B*). When RyRs are close to the PSD (head), the opening probability is highest (32.22% ± 5.95%), and when the RyRs are located further from the PSD, the RyR opening probability decreases (in the lower neck configuration, 8.91% ± 3.64%). Next we studied the effect of different RyR distributions along the SA on the Ca^{2+} dynamics in both the spine and the dendrites (Fig. 3*C*). Figures 3*C.i* and *C.ii* show the Ca^{2+} dynamics of a single seed for each RyR distribution in the spine and in the dendrite (Fig. 2*F*), respectively. In general we observe that the spine has higher Ca^{2+} than the dendrite in these simulations.

We next separated the cases where the RyRs open ($\mathbf{n}$, Fig. 3*D*) versus closed ($\mathbf{N}\backslash\mathbf{n}$, Fig. 3*E*) to understand how different sources and sinks contribute to Ca^{2+} dynamics. The Ca^{2+} averaged over all simulations $\mathbf{N}$ is a combination of the subset of simulations with open and closed RyRs weighted by their opening probability. To quantify the differences in the Ca^{2+} ion curves, we performed ANOVA and Tukey's test at timesteps 15, 22.5 and 30 ms between the different distributions and the head distribution. As expected, in the simulations in $\mathbf{n}$, the cytosolic Ca^{2+} in the spine is significantly higher than in the case when the RyRs remain closed (compare Fig. 3*D.i* and *E.i*). When the RyRs are located closer to the PSD (head and homogeneous cases), Ca^{2+} is higher in the spine region and more RyRs tend to open, which through CICR leads to a higher Ca^{2+} peak in the spine (Fig. 3*D.i*). This trend is reversed in the case when the RyRs do not open $\mathbf{N}\backslash\mathbf{n}$ (Fig. 3*E.i*) because in this case, RyRs merely act as Ca^{2+} buffers. As we will see later buffering plays an important role in modulating Ca^{2+} dynamics in the spine. Next we analysed the differences in Ca^{2+} number in the dendrite based on RyR localization (Fig. 3*D.ii* and *E.ii*). The amount of Ca^{2+} in the dendrite serves as a marker for synaptic transmission (Regehr & Tank, 1990). In general fewer Ca^{2+} ions are observed in the dendrite than in spines due to buffering (compare left and right panels in Fig. 3*D* and *E*). In the simulations with open RyR $\mathbf{n}$, the highest number of Ca^{2+} ions in the dendrite corresponds to the lower neck RyR distribution, followed by the neck distribution. In the case where RyRs are localized to the head, a significantly lower amount of Ca^{2+} reaches the dendrite (Fig. 3*D.ii*). As expected, in cases where the RyRs remain closed, the trends for Ca^{2+} in the dendrites are reversed (Fig. 3*E.ii*).

To further analyse these Ca^{2+} trends numerically, we computed the mean and standard error of the mean for the maximum value of Ca^{2+} ions for each single simulation both in the spine (Fig. 3*F*) and in the dendrite (Fig. 3*G*). We observed that for the cases where RyRs were open, high Ca^{2+} in the spine is achieved when RyRs are in the head (1306.3 ± 50.02 in the head compared to 902.2 ± 62.52 in the low neck) and high Ca^{2+} reaches the dendrite when the RyRs are located in the neck (71.2 ± 6.38 in the head compared to 211.2 ± 21.96 in the low neck). In the

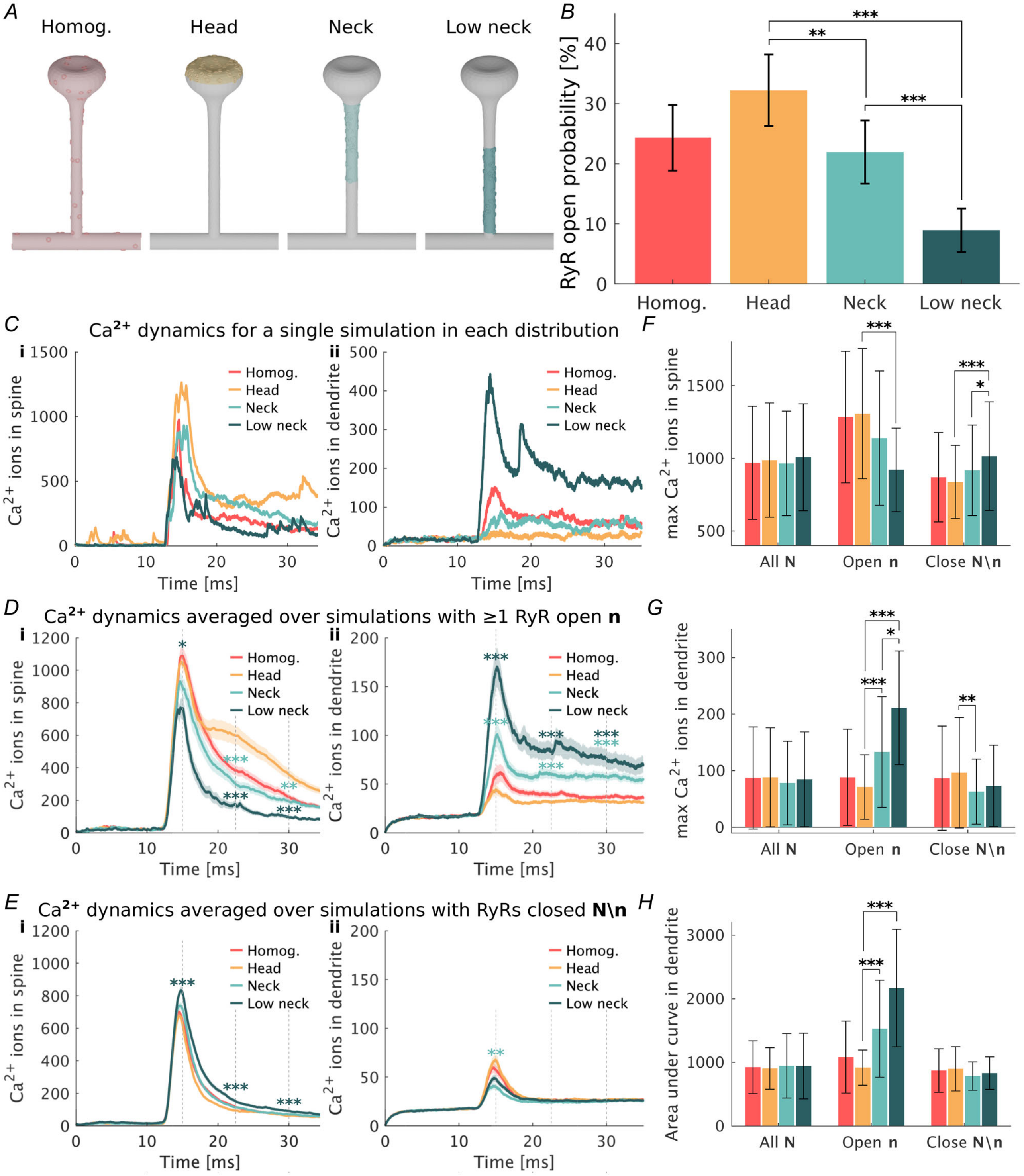

Figure 3. Effect of RyR distribution on Ca^{2+} dynamics in idealized spine and non-laminar SER

(A) Distributions of RyR considered in idealized SER geometries. (B) RyR opening probability for each distribution, defined as the percentage of simulations containing at least one opened RyR. The bars represent the maximum likelihood estimate of the opening of the RyRs. A total of **N** = 250 simulations were run. The *p*-values for the RyR opening probability were calculated from Fisher's exact test. (C) Number of Ca^{2+} ions in the spine (left) and dendrite (right) for a single simulation. (D) Number of Ca^{2+} ions in the spine (left) and dendrite (right) for those simulations containing at least one RyR opened **n** ($\mathbf{n}_{\mathbf{homog}}$ = 60, $\mathbf{n}_{\mathbf{head}}$ = 80, $\mathbf{n}_{\mathbf{neck}}$ = 54 and $\mathbf{n}_{\mathbf{lowneck}}$ = 21). (E) Number of Ca^{2+} ions in the spine (left) and dendrite (right) for those simulations containing closed RyRs **N\n**. (F)

Max number of Ca^{2+} ions at the spine calculated for each simulation. (G) Max number of Ca^{2+} ions at the dendrite calculated for each simulation. (H) Area under the curve for number of Ca^{2+} ions reaching the dendrite (D, E right panels). In plots (D) and (E), mean and standard error of the mean are shown. Kruskal–Willis and Dunn–Šidák's test was performed at times 15, 22.5 and 30 ms with respect to the head distribution. For plots (F)–(H), mean and standard deviation are shown and the *p*-values are calculated with Kruskal–Willis and Dunn–Šidák's test. Statistically significant differences are indicated as $^{*}P < 0.05$, $^{**}P < 0.01$ and $^{***}P < 0.001$.

closed cases, the opposite trend is observed, with more Ca^{2+} ions reaching the dendrite when the RyRs are in the head (96.4 ± 7.49 in the head compared to 73.3 ± 4.75 in the low neck) even though there are lower number of ions in the spine (837.0 ± 19.29 in the head compared to 1014.7 ± 24.64 in the low neck). The total number of Ca^{2+} ions reaching the dendrite, as indicated by the area under the curve of ions, also showed the same trends (compare Fig. 3*G* and Fig. 3*H*). Thus our results suggest that the location of RyR plays a critical role in determining the spatial impact of RyR opening probability and CICR, thereby affecting spine and dendrite Ca^{2+} concentrations. The differences in dendrite Ca^{2+} concentrations based on RyR location can have implications for neuronal downstream signalling.

IP_3R located at the dendrite and RyR in the spine neck maximize the number of Ca^{2+} ions reaching the dendrite

The previous results show that placing the RyRs towards the neck is more efficient in terms of maximizing the number of Ca^{2+} ions reaching the dendrite from the spine. We next wanted to understand whether there exists a positional advantage to placing IP_3Rs at the dendrite, as measured in experimental data by Sharp et al. (1993), instead of a homogeneous distribution. Therefore, we included the IP_3R model from De Young and Keizer (1992) as suggested by Singh et al. (2021). We ran simulations using two different IP_3R distributions in the idealized plasma membrane with idealized ER geometry, one assuming homogeneous IP_3R distribution throughout the entire ER and one assuming IP_3R localization at the dendrite (Fig. 4*A*). A slightly higher, but non-significant, number of Ca^{2+} ions was measured in the spine when assuming a homogeneous distribution of IP_3Rs compared to localizing the IP_3Rs at the dendrite; see Fig. 4*A.i*. However localization of IP_3Rs at the dendrite results in a higher number of Ca^{2+} ions reaching the dendrite; see Fig. 4*A.ii* and *A.iii*.

To further analyse the interplay between RyR and IP_3R and the effect of their localization on Ca^{2+} signalling, we ran simulations assuming the IP_3R to be localized at the dendrite as measured experimentally by Sharp et al. (1993) while varying the RyR localization. The observations from Fig. 3 were maintained when including IP_3Rs, that is, more Ca^{2+} reached the dendrite when the RyRs were localized at the neck of the SA; see Fig. 4*B.ii* and *B.iii*. We also distinguished between simulations where only the IP_3Rs opened and simulations where both IP_3Rs and RyRs opened, Fig. 4*B*. Simulations in which both receptor types opened led to a higher number of Ca^{2+} ions both in the spine and in the dendrite. Furthermore placing the IP_3Rs in the dendrite and the RyRs in the neck led to more Ca^{2+} ions reaching the dendrite; see Fig. 4*B.iii*. These results show that the spatial localization of IP_3Rs and RyRs measured in experimental data maximizes efficiency in spine-to-dendrite communication from a Ca^{2+} handling perspective.

RyR localization in the neck increases Ca^{2+} in the dendrite in a realistic plasma membrane geometry

Next we sought to understand how changing the plasma membrane geometry would affect the opening probability of NMDAR (Fig. 5). In the realistic PM geometry, there are two PSDs (Fig. 5*A*) compared to one PSD in the idealized PM geometry. We first simulated one PSD at a time in the realistic geometry (Fig. 6*E*). We found that this resulted in few NMDAR opening and therefore decided to stimulate both PSDs simultaneously to ensure sufficient Ca^{2+} influx into the spines. We used a model that allows NMDAR to exist in different states based on Ca^{2+} binding and glutamate binding Fig. 5*B*. Both receptor density and glutamate to NMDAR ratio were kept constant throughout the simulations with realistic and idealized PM as shown in Table 6. We found that the opening probability of NMDAR was significantly higher in the idealized PM than in the realistic PM (Fig. 5*C*). We conducted simulations in both geometries with only NMDAR (without AMPAR) to understand why this was happening. When analysing the different NMDAR states in both the realistic and the idealized plasma membranes, we observed that the activation of C2 state of the NMDAR model was much lower in the realistic plasma membrane configuration compared to the idealized plasma membrane (Fig. 5*D*). Furthermore, when analysing the average number of NMDAR molecules at state C1 and C2, the idealized PM showed much higher numbers than the realistic PM (Fig. 5*F*), despite having a lower initial total number of NMDAR receptors at state C0 (Table 6). This indicates that glutamate binding to the NMDARs is reduced in the realistic plasma membrane than in the idealized configuration due to geometric factors.

The only difference between both sets of simulations is the geometry of the PM and the presynaptic membrane. The PSDs in the realistic plasma membrane are less concave and more elliptical than the PSD in the idealized plasma membrane; see Fig. 6. To quantify the curvatures, we calculated the first principal curvature k_1 of both the idealized and the realistic PSD (see Fig. 6*A* and *C*) using GaMER2 (Lee et al., 2020). We observed very different histograms for the PSDs, with more variable curvatures in the realistic PSDs. In addition the idealized PSD has an averaged k_1 value of 8.07 μm^{-1}, whereas the two realistic PSDs have averaged k_1 values of 4.58 and 7.07 μm^{-1}, respectively. Furthermore, we considered the synaptic volume, determined by considering the presynaptic membrane and the PSD as a closed volume and calculating the surface area to volume ratios. This calculation was performed to quantify the shape of the whole synapse, because the surface of the presynaptic membrane might also affect the diffusion and, therefore, opening probabilities. The surface area to volume ratio calculations showed that, in the idealized geometry, this metric was nearly doubled in comparison to the realistic PSDs (see Fig. 6*B*). A higher surface area to volume ratio allows the diffusion of particles to reach the membrane faster. PSD 1 had a lower averaged curvature value and a lower surface area to volume ratio than PSD 2. Therefore, to further test the hypothesis that the shape of the presynapse and the curvature of the PSD can impact NMDAR opening probability, we ran simulations only activating PSD 1 or PSD 2. We observed that PSD 2 activation led to a higher NMDAR opening probability than PSD 1 activation (see state 'O' in Fig. 6*E*) suggesting that higher curvature and higher surface to volume ratios were favourable for NMDAR opening.

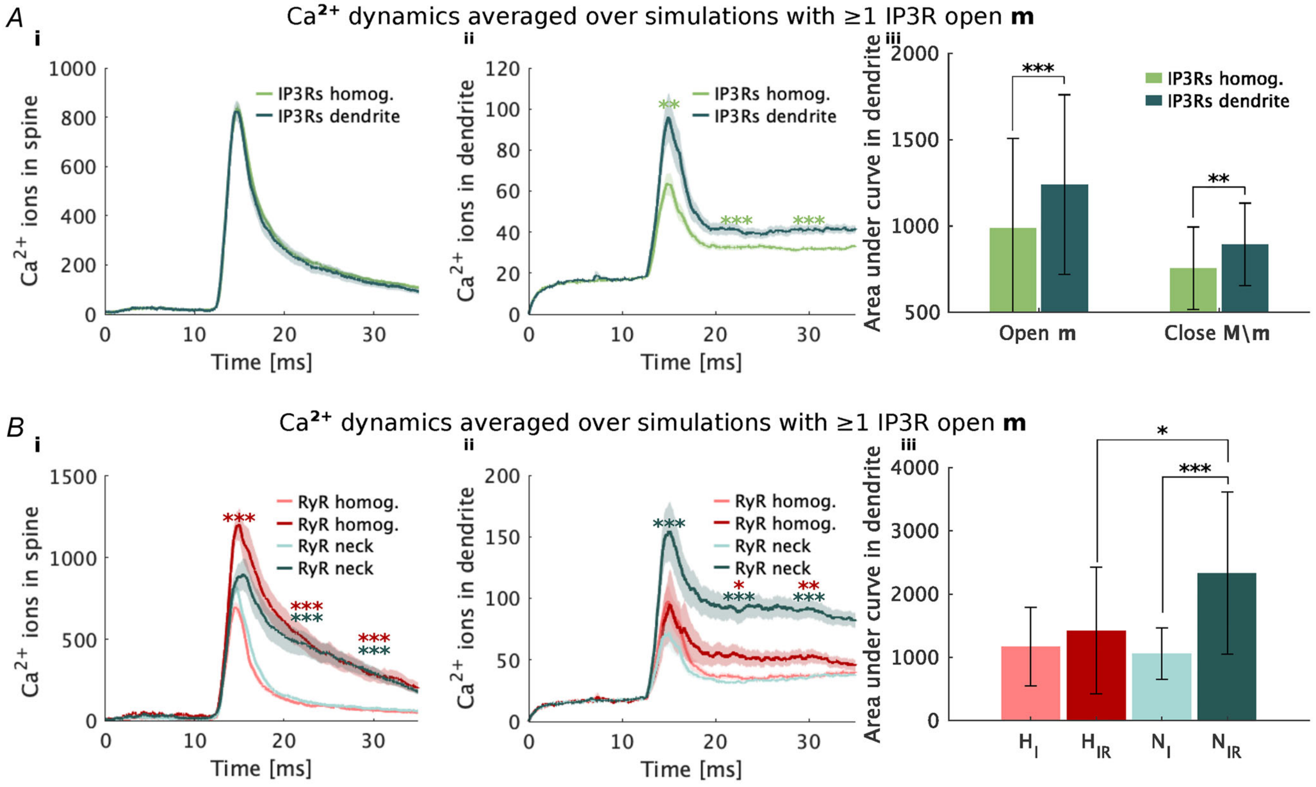

Figure 4. Effect of RyR and IP_3R distribution on Ca^{2+} dynamics in idealized spine and non-laminar SER
(A) Number of Ca^{2+} ions in the spine (left) and dendrite (centre) when IP_3Rs are located in the dendrite or homogeneously distributed throughout the SA. On the right, area under the curve for number of Ca^{2+} ions reaching the dendrite. (B) Crosstalk between IP_3Rs distributed in the dendrite and RyRs located at the neck of the spine. Number of Ca^{2+} ions in the spine (left) and dendrite (centre) depending on the location of both IP_3Rs and RyRs. Darker shades represent simulations where both IP_3Rs and RyRs open, whereas lighter shades represent simulations where only the IP_3Rs open. On the right, area under the curve for number of Ca^{2+} ions reaching the dendrite. H and N represent the RyRs localized homogeneously and in the neck respectively, whereas the sub-indices I and R represent whether the IP_3Rs or the RyRs open. In plots in the left and the centre, mean and standard error of the mean are shown. Kruskal–Willis and Dunn–Šidák's test was performed at times 15, 22.5 and 30 ms with respect to the head distribution. For plots on the right side, mean and standard deviation are shown, and the *p*-values are calculated with Kruskal–Willis and Dunn–Šidák's test. Statistical significance is indicated by $*P < 0.05$, $**P < 0.01$ and $***P < 0.001$.

Using this realistic PM geometry from mouse cerebral cortex spines (Lee et al., 2020; Wu et al., 2017), we next studied the effects of RyR localization. We smoothed out the measured realistic SA head (Fig. 1*C.iv*) to obtain a non-laminar ER head (Fig. 1*C.iii*) and kept the realistic ER in neck and dendrites. This allows us to assume a non-laminar SER and run simulations that are comparable to our non-laminar SER and idealized plasma membrane configuration. In this case we used three RyR distributions: Homog., Head and Neck, eliminating 'low neck' due to the thin neck geometry. We found that in this hybrid SA geometry, the opening probability of RyRs $P(\mathbf{n})$ still strongly depends on the RyR localization, but is different from the idealized geometry. In this case, the highest opening RyR probability 36% ± 6% was obtained when concentrating the RyRs towards the neck of the SA, followed by the head (24% ± 5%) and the homogeneous distribution (18% ± 5%). Both the homogeneous and head distributions showed a statistically significant lower opening probability when compared to the neck distribution. A potential explanation lies in the fact that fewer NMDARs are opened in the realistic PM than in the idealized PM (see Fig. 5*C*). We also calculated the shortest Euclidean distance from every point in the triangulated mesh of the PSD to the ER and calculated the mean distance over each point (see Fig. 7). The PSD-to-ER distance was significantly higher in the realistic PM than in the idealized one, thus indicating that Ca^{2+} ions need to traverse a higher distance while exposed to Ca^{2+} buffering before reaching the ER. The lower NMDAR opening probability combined with the higher PSD-to-ER distance in the realistic PM helps explain why the neck distribution leads to higher RyR opening probabilities.

Increased ER laminarity decreases RyR opening probability and Ca^{2+} concentration in the spine

The ER in neurons is highly dynamic, and it has been shown to enter and exit spines in an activity-dependent manner (Konietzny et al., 2022). Recently Perez-Alvarez et al. (2020) showed that transient ER visits in dendritic spines were mostly synaptopodin negative, whereas 90% of the spines containing stable ER were synaptopodin positive. This suggests that a SA, whose characteristic laminar SA shape is highly related to synaptodopin (Konietzny et al., 2022), is more likely to be present in ER stable spines, whereas transient ER visits in spines are more likely to manifest a non-laminar SER. To investigate how the laminarity of the SA would impact Ca^{2+} dynamics, we next simulated ER geometries with laminarities and compared them against non-laminar SER geometries. We first conducted simulations with the

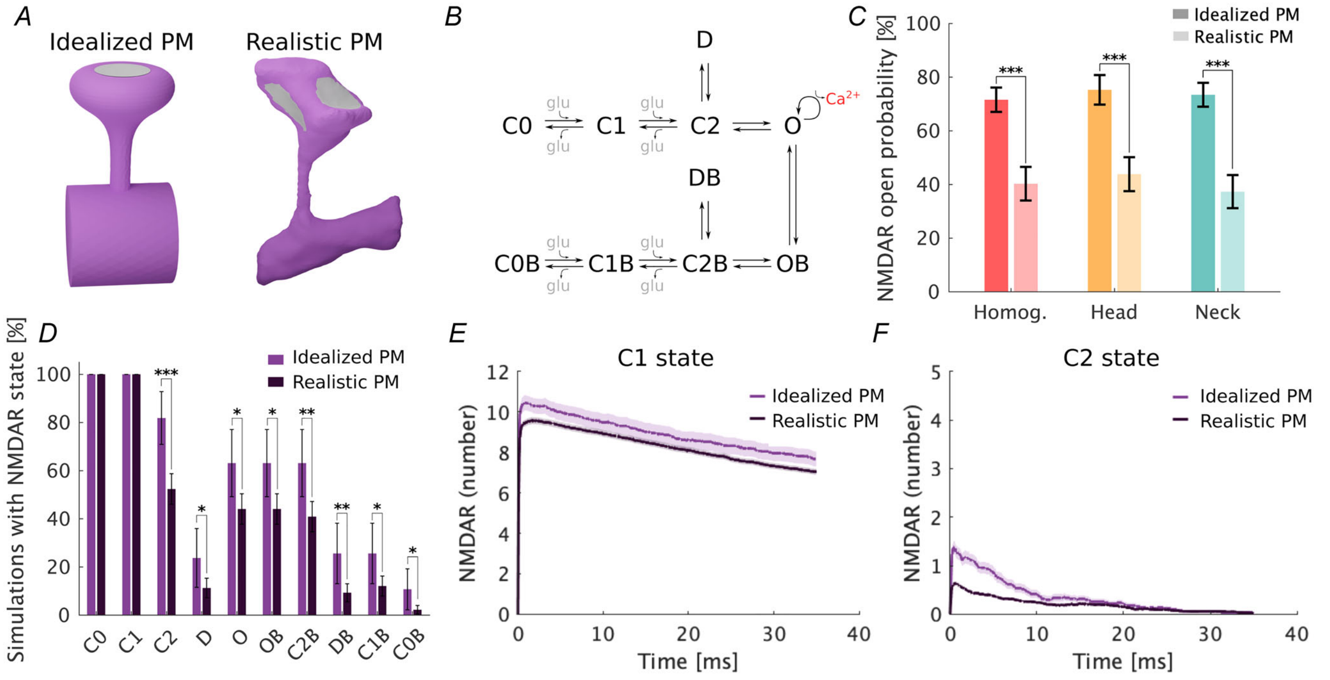

Figure 5. Effect of plasma membrane geometry on NMDAR opening
(A) Idealized and realistic plasma membrane geometries with the PSD area marked in grey. (B) Schematic of NMDAR reaction rate model. (C) NMDAR opening probability for the idealized and realistic plasma membrane geometry. (D) Probability of each NMDAR state per reaction. The *p*-values were calculated using a two sample *t*-test. Statistically significant differences are indicated as $^{*}P < 0.05$, $^{**}P < 0.01$ and $^{***}P < 0.001$. (E) Averaged number of NMDAR in state C1. (F) Averaged number of NMDAR in state C2.

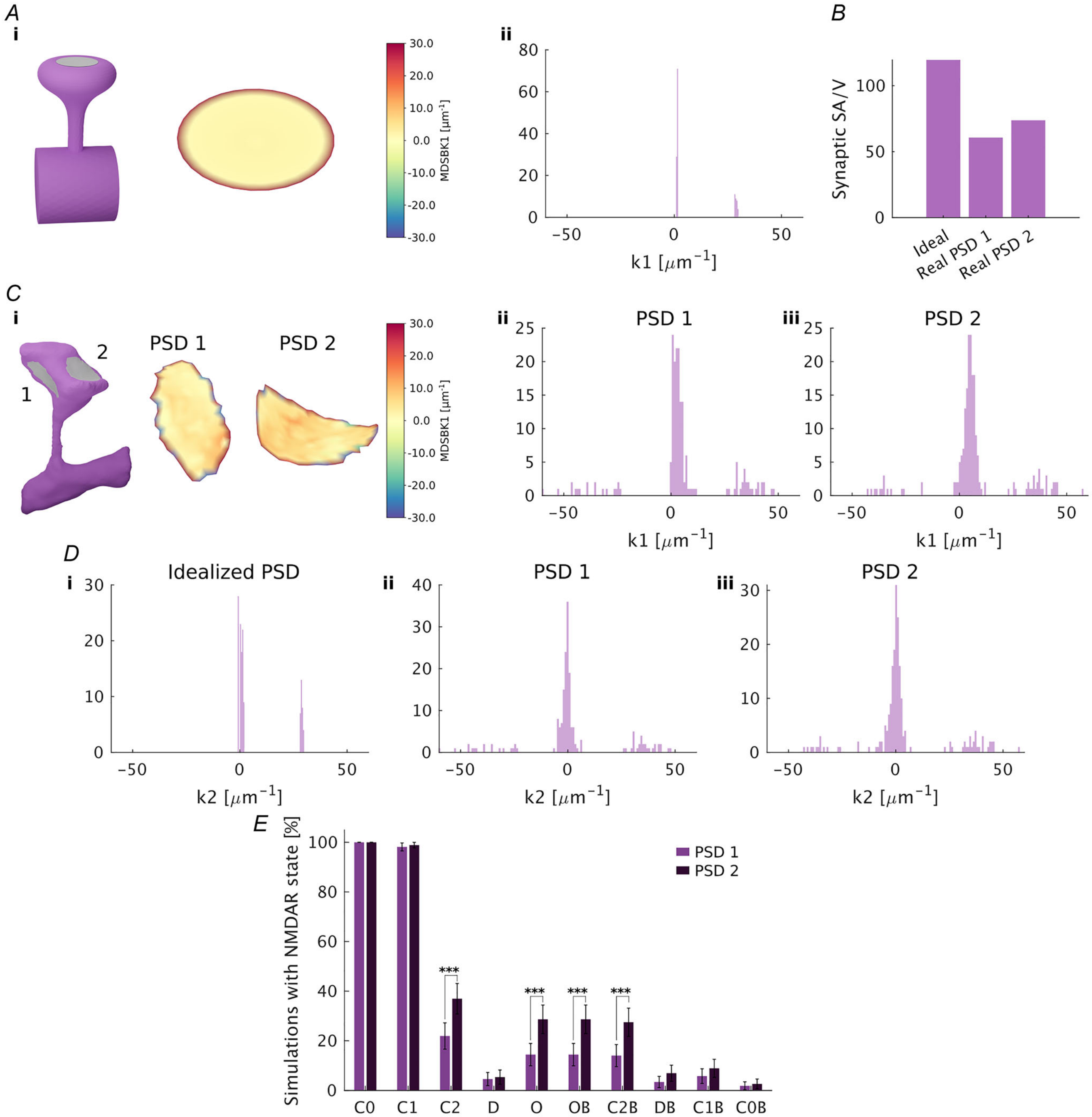

Figure 6. Analysis of the PSD curvature in the idealized and realistic PSDs

(A) $k1$ curvature value calculated for the idealized PSD (shown in grey on spine geometry, left image) and the histograms of the $k1$ distribution at each triangle of the mesh. (B) Surface area to volume ratio calculated for the closed synaptic space. (C) $k1$ curvature value calculated for the realistic PSDs (shown in grey on spine geometry, left image) and the histograms of the $k1$ distribution at each triangle of the mesh. (D) $k2$ curvature histograms value calculated for the idealized PSD, PSD1 and PSD2 in the realistic geometry. (E) Probability of each NMDAR state per reaction. The p-values were calculated using a two sample t-test. Statistically significant differences are indicated as $^{*}P < 0.05$, $^{**}P < 0.01$ and $^{***}P < 0.001$.

realistic plasma membrane combined with the realistic laminar SA measured by Wu et al. (2017); see Fig. 1*C.iv*. The SA geometry was segmented and meshed by Lee et al. (2020). Ca^{2+} was able to penetrate the ER laminar layers. We found that when the ER has a laminar geometry (SA), a higher opening probability is observed when the RyRs are located towards the neck (Fig. 8*B*), similar to observations in the non-laminar SER geometry. We found that the proportion of open RyR simulations containing opened NMDARs was quite low (Fig. 8*F*), as was the case in the realistic plasma membrane with non-laminar SER geometry. Figure 8*C* shows examples of single-simulation Ca^{2+} dynamics for each RyR configuration both in the spine (Fig. 8*C.i*) and in the dendrite (Fig. 8*C.ii*). In cases where the RyRs open (**n**), the neck set-up leads to a significantly lower number of Ca^{2+} ions in the spine (Fig. 8*D.i*) than when the RyRs are localized to the head or when they are homogeneously distributed. However this effect is reversed when considering how much Ca^{2+} reaches the dendrites, with the head RyR localization having the lowest Ca^{2+} in the dendrite (Fig. 8*D.ii*). This significant difference was also observed when analysing the total number of Ca^{2+} (area under the curve) in the dendrites (Fig. 8*G*). In this case there are also long time differences in Ca^{2+} in the dendrites in the homogeneous configuration, suggesting that there is a cross talk between RyR localization, Ca^{2+} in the spine and Ca^{2+} in the dendrite. We also tested the effect of placing the IP_3Rs in the dendrite. In simulations with both RyRs and IP_3Rs opened, maximal Ca^{2+} reached the dendrite (Fig. 8*E.ii* and *H*).

Non-laminar tubules of SER enter dendritic spines (Konietzny et al., 2022), whereas in more mature and stable spines, the characteristic laminar SA structure is observed (Perez-Alvarez et al., 2020; Spacek & Harris, 1997). This physiological differences between nascent ER and mature SA motivated us to study whether there are any differences in spine-to-dendrite communication based on geometrical properties of the ER in the dendritic spines. To fully understand the effect of laminarity, we directly compared simulations of laminar and non-laminar ER structures (Fig. 9) for different PM geometries. In all cases the RyR number was kept constant, as was the SERCA density. We found that the RyR opening probability was lower in the laminar case than in the non-laminar case for all distributions of RyR (Fig. 9*A*). As a result, the maximum Ca^{2+} in the spines was also lower in the laminar case when compared to the non-laminar case (Fig. 9*B.i*, *Bii* and *C*). We further investigated the different sources and sinks of Ca^{2+} in the spine. One of the main changes that comes with adjusting SA laminarity is surface area of the membrane. SERCA density was held constant across the different simulation set-ups. The SERCA density value was chosen from Bell et al. (2022), and SERCA was homogeneously distributed throughout the SA. Due to a higher surface area in the laminar part of the SA, a higher absolute number of SERCA was located in the laminar region. Figure 10 shows that the specific SERCA location within the SA matches the experimental results from Basnayake et al. (2019). As a result, more Ca^{2+} is pumped back into the SA in the laminar case, whereas increased Ca^{2+} in the spine is observed in the non-laminar case. To understand these effects, we ran simulations on non-laminar and laminar ER containing only SERCA and no RyR and the same effects were observed (Fig. 11*A*).

However there is no change in the Ca^{2+} in the dendrite because of Ca^{2+} buffering by mobile and immobile buffers (Fig. 11*B*). Furthermore, when the number of SERCA, rather than the density, is kept the same in the laminar and non-laminar geometries, we found that these spatial effects were eliminated (Fig. S8*C*). Thus our analysis suggests that the complex Ca^{2+} dynamics are not simply modulated by geometric factors such as surface-to-volume ratio but rather the balance

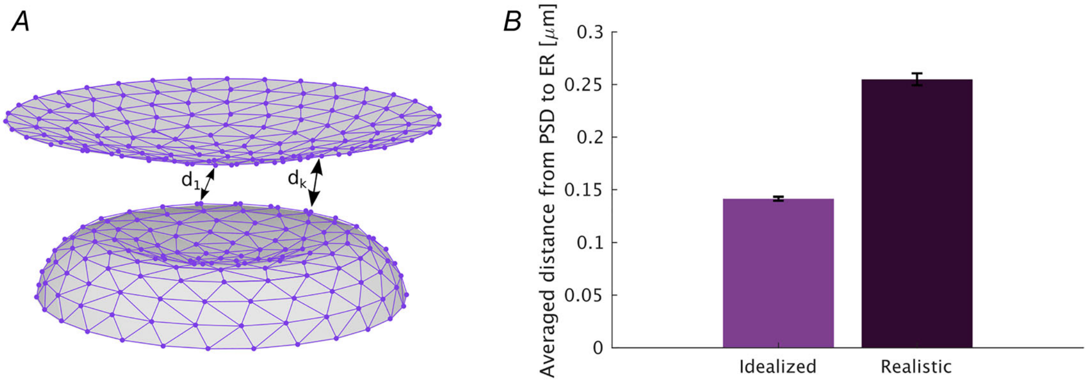

Figure 7. Averaged minimum Euclidean distance between each point of the PSD and the ER
(A) For each point in the PSD mesh, the Euclidean distance to each point in the ER mesh was measured. The shortest distance for each node was then kept. The average of the shortest distance was then computed. (B) The averaged shortest Euclidean distance between PSD and ER was calculated for both the idealized and the realistic PM.

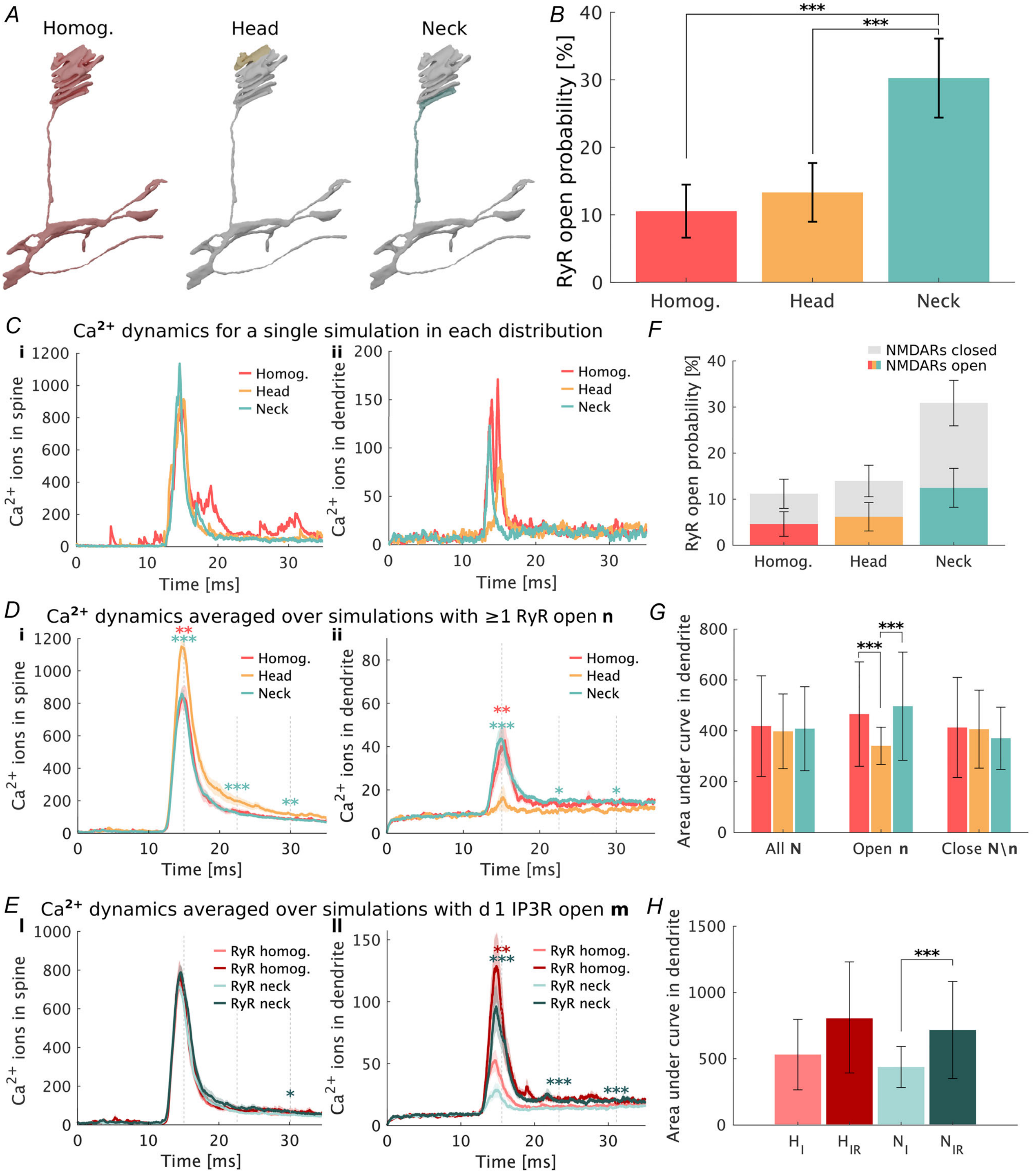

Figure 8. Effect of RyR localization on realistic plasma membrane and laminar SA

(A) RyR distributions considered in the realistic SA geometries. (B) RyR opening probability for each distribution set-up. The bars represent the maximum likelihood estimate of the opening of the RyRs. The *p*-values for the RyR opening probability where calculated from Fisher's exact test. (C) Number of Ca^{2+} ions in the spine (left) and dendrite (right) for a single simulation. (D) Number of Ca^{2+} ions in the spine (left) and dendrite (right) for those simulations containing at least one RyR opened **n**. (E) Number of Ca^{2+} ions in the spine (left) and dendrite (right) for those simulations containing no open RyRs **N\n**. (F) RyR opening probability for each distribution including how many of the simulations contain opened NMDARs and how many closed NMDARs. (G) Area under the curve for number of Ca^{2+} ions in spine. (H) Area under the curve for number of Ca^{2+} ions reaching the dendrite (D, E right panels). In plots (D) and (E), mean and standard error of the mean are shown. Kruskal–Willis and Dunn–Šidák's test was performed at times 15, 22.5 and 30 ms with respect to the head distribution. For plots (G) and (H), mean and standard deviation are shown and the *p*-values are calculated with Kruskal–Willis and Dunn–Šidák's test. Statistically significant differences are indicated as $^{*}P < 0.05$, $^{**}P < 0.01$ and $^{***}P < 0.001$.

between sources and sinks on different surfaces and volumes. When we now compare the Ca^{2+} in spines with either idealized PM or realistic PM, we find that spine Ca^{2+} is higher in the non-laminar case than in the laminar case (Fig. 9*C*). Conversely when RyRs are concentrated at the neck, the laminar SA structure leads to non-statistically significant more Ca^{2+} reaching the dendrite compared to non-laminar geometries (Fig. 9*D*). Thus our simulations predict that laminar SA structure is effective at maintaining Ca^{2+} concentration in the dendrite constant. This may have potential consequences for how spines communicate with one another.

Discussion

In this work we sought to decipher the role of the ER in regulating spine and dendrite Ca^{2+} dynamics. However this is a complex problem where one needs to consider the geometry of the spine and the geometry of the ER itself. In some nascent spines, transient SER are dominant, whereas more mature spines tend to contain a specialized form of the SER, the SA. The precise functional differences between the SER and the SA remain elusive. Morphological changes in the SA have been observed after the induction of long-term potentiation (LTP) (Chirillo et al., 2019; Jedlicka et al., 2008), and ER disturbances have been seen in a number of neurodegenerative disorders (Hetz & Mollereau, 2014).

Here we implemented a stochastic particle-based model of Ca^{2+} transients in dendritic spine to understand how RyR distributions on the SER and SA, as well as ER laminarity, affect Ca^{2+} dynamics. The model was implemented on an idealized spine plasma membrane as well as on a realistic spine re-constructed from hippocampal rat neurons (Lee et al., 2020; Wu et al., 2017).

First, to disentangle the contribution of membrane geometry on Ca^{2+} dynamics, we use both an idealized spine plasma membrane and an idealized SER. We found that RyR distribution impacts the likelihood of RyR opening and Ca^{2+} dynamics. Variations in RyR open probabilities and Ca^{2+} responses are influenced by geometrical and biophysical factors. RyRs located in the head region exhibit higher local Ca^{2+} concentrations due to their proximity to NMDARs at the PSD, as shown in Fig. 3. However, in Fig. 6, RyRs in the head region display reduced opening probabilities, likely due to the increased distance between the ER and the plasma membrane, as illustrated in Fig. 7. Overall, independently of ER to plasma membrane distance, our model predicts that distributing the RyRs towards the neck of the ER, as they have been suggested to be preferentially located (Basnayake et al., 2019), results in a higher peak Ca^{2+} and total number of Ca^{2+} ions reaching the dendrite if the RyRs open, whereas concentrating RyRs in the head results in higher spine Ca^{2+} but a lower number of ions reaching the dendrite. In addition we have observed significant differences in NMDAR opening probability due to purely geometrical properties (see Fig. 5*C* and *D*). Glutamate release was initiated at the centre of the presynaptic membrane, and its diffusion dynamics were simulated to facilitate NMDA receptor (NMDAR) activation. We acknowledge, however, that the fact that the geometry of the synaptic cleft plays a critical role on NMDAR activation is of high relevance for synaptic activity. To address this we conducted a separate study examining how variations in synaptic cleft geometry influence glutamate diffusion and receptor activation. The findings of this analysis are detailed in a separate manuscript (Hernandez Mesa et al., 2025).

Our conclusions are compatible with previous computational models. Breit et al. (2018) found that RyRs and RyR positioning (by varying SER position) affect spine-to-dendrite communication. Our results on the efficiency of localizing the RyRs towards the neck match previously reported results in a computational study replicating a Ca^{2+} uncaging stimulus (Basnayake et al., 2019). Our model expands these conclusions from previous computational studies by studying the effect of different RyR distributions in laminar and non-laminar SER geometries from both idealized and realistic meshes. Furthermore we assume a physiological stimulus including both glutamate release and membrane depolarization from bAP and EPSP. In addition all the receptors and channels in our model included kinetic models of activation with parameters either measured experimentally or fitted to experimental data. In contrast to other stochastic simulation models (Breit et al., 2018; Basnayake et al., 2019; Holcman et al., 2004), we include additional receptors and channels, our stimulus is physiological and our parameters are based on experimental data. A larger amount of Ca^{2+} reaching the dendritic shaft could have downstream consequences activating other organelles in the dendrite as well as in spine-to-spine communication or spine clustering (Harris, 2020). This becomes especially important when we consider the fact that SA is found in more mature spines, which tend to be clustered close to smaller spines. We found that the trends in Ca^{2+} are consistent and statistically significant throughout the different geometries distributing the RyRs towards the neck or head.

Interestingly opposite trends were observed on simulations where the RyRs stayed closed, with more Ca^{2+} reaching the dendrite if the RyRs were located towards the head of the ER. These differences between open and closed RyRs are related to the fact that RyRs are activated through CICR. Thus RyRs act as a Ca^{2+} source when activated, but as a Ca^{2+} buffer if they remain closed. A further takeaway is the effect of the plasma membrane geometry on RyR opening probability. The shape of the plasma membrane has an effect on glutamate binding to the NMDARs. Whereas the simulations with opened RyRs in the idealized plasma membrane

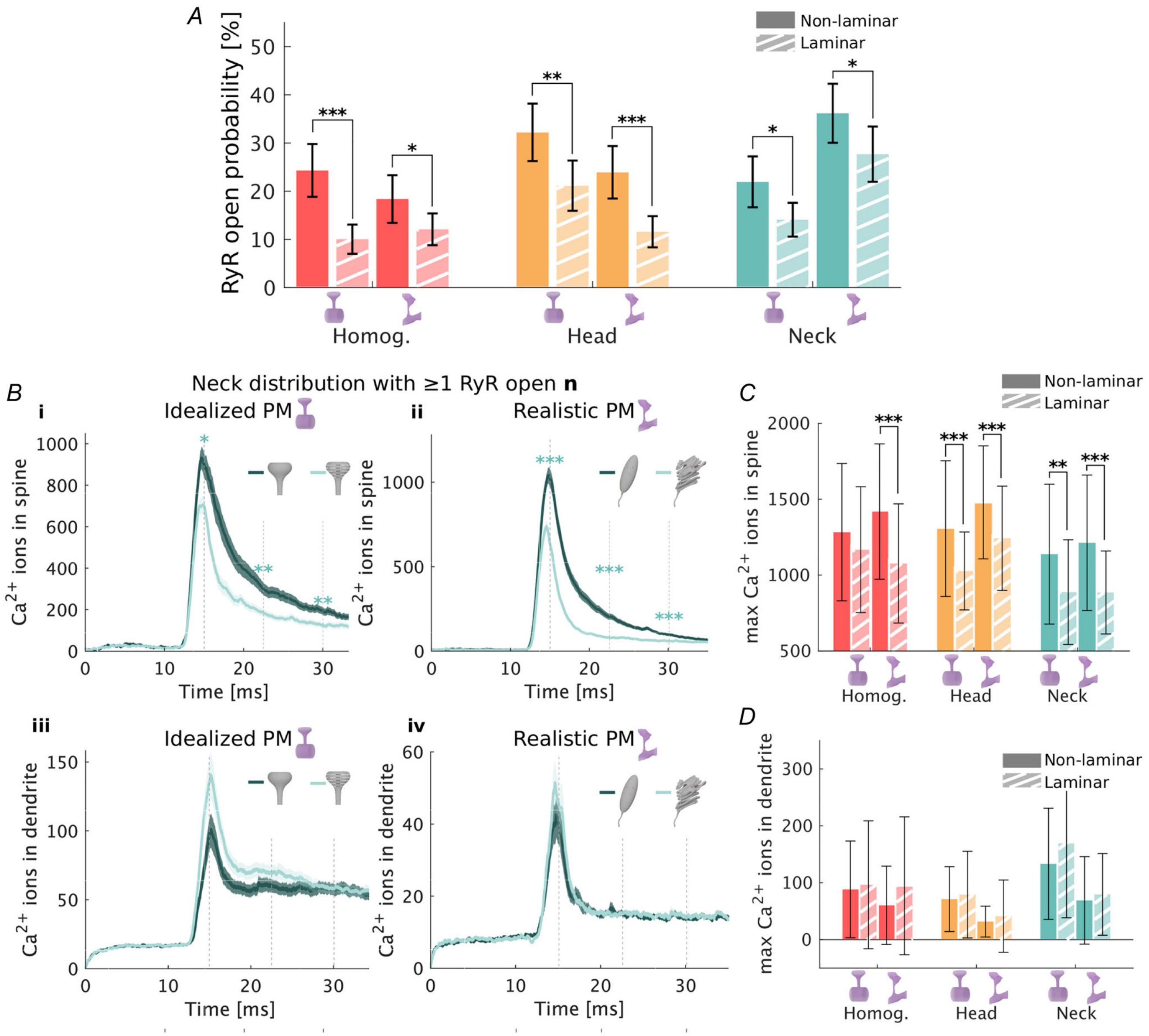

Figure 9. Comparison between a non-laminar SER and a laminar spine apparatus for both plasma membrane geometries

(A) RyR opening probability comparing non-laminar SER and laminar SA for both plasma membrane geometries. (B) Comparison between number of Ca^{2+} ions assuming non-laminar and laminar ER in the spine (i and ii) an in the dendrite (iii an iv) for both idealized (i an iii) and realistic plasma membrane geometries (ii and iv). Mean and standard error of the mean are shown. A two sample *t*-test was performed at times 15, 22.5 and 30 ms. (C) Maximum number of Ca^{2+} ions at the spine calculated for each simulation. (D) Maximum number of Ca^{2+} ions at the dendrite calculated for each simulation. For plots (C) and (D), mean and standard deviation are shown, and the *p*-values are calculated with a Mann–Whitney *U* test. Statistically significant differences are indicated as $^{*}P < 0.05$, $^{**}P < 0.01$ and $^{***}P < 0.001$.

contained mostly opened NMDARs, this was not the case in simulations in the realistic plasma membrane, where most of the RyR activation occurred via Ca^{2+} influx through the VSCCs. As a result, the realistic plasma membrane showed the highest RyR opening probability when placing the RyRs towards the neck of the ER. Imaging experiments have shown that VSCC-mediated Ca^{2+} influx dominates the Ca^{2+} dynamics in dendritic spines (Magee & Johnston, 1997; Yasuda et al., 2003; Yuste & Denk, 1995), as was the case in simulations with realistic plasma membrane geometries. The fact that a higher RyR neck opening probability is achieved when VSCC Ca^{2+} influx dominates further emphasizes the importance of RyR localization towards the neck to improve spine-to-dendrite communication. In addition our simulations with IP_3Rs show that placing the IP_3Rs at the dendrites combined with RyRs placed in the spine neck, as measured experimentally by Basnayake et al. (2019) and Sharp et al. (1993), is an efficient way of increasing the number of Ca^{2+} ions reaching the dendrite from the spine.

Furthermore the laminarity of the SA affects both the opening probability of the RyRs and the Ca^{2+} transients. In both idealized and realistic plasma membranes, we observed that ER laminarity (a common characteristic of mature SA geometries) leads to a lower RyR opening probability and a slightly higher, statistically non-significant, number of Ca^{2+} ions reaching the dendrite. This result is an outcome of the complex interplay between geometry, SERCA and Ca^{2+} buffers. Although a detailed understanding of the mechanisms of the ER anchoring to the dendritic spine and the formation of SA still remains elusive (Falahati et al., 2022; Konietzny et al., 2022), recent studies have shown that spines with transient ERs were mostly synaptopodin negative, whereas synaptopodin was detected in 90% of stable ER spines (Perez-Alvarez et al., 2020). This, together with the fact that synaptopodin contributes to the characteristic laminar disc structure of SA (Falahati et al., 2022), suggests that laminar SA are more related to stable ER spines than non-laminar ER geometries. The outcomes of our study give further insight into the effects and differences between laminar and non-laminar ER structures on Ca^{2+} transients, and provide evidence that mature, laminar SA structures are more likely to facilitate efficient spine-to-dendrite communication.

We acknowledge that the use of the standard error of the mean in our figures has limitations, as it decreases inversely with the square root of the number of simulations **N** and does not directly represent the variability of individual data points. However our choice to use standard error of the mean was intentional, aimed at providing a concise representation of the precision of the mean to facilitate clearer comparisons of central trends across conditions. Although standard deviations are better suited for illustrating data variability, SEM is particularly useful when the focus is on comparing group means, as in our study. In our previous work (Bell et al., 2022), SD was used, but during the early stages of this study, we found that SEM allowed for a more straightforward comparison of central trends. To address potential concerns, we have included raw calcium signal data for selected figures in Fig. 12, providing a clearer view of the data distribution and variability. As shown in Fig. 13, these data illustrate distinct differences between head and neck responses under various conditions, offering additional insight into the underlying variability.

One limitation of our study is related to the gating rates of the RyR model used. The RyR model was taken from Tanskanen et al. (2007), which was designed to replicate RyR dynamics in cardiac myocytes. However, due to the difficulty of measurements in small volumes

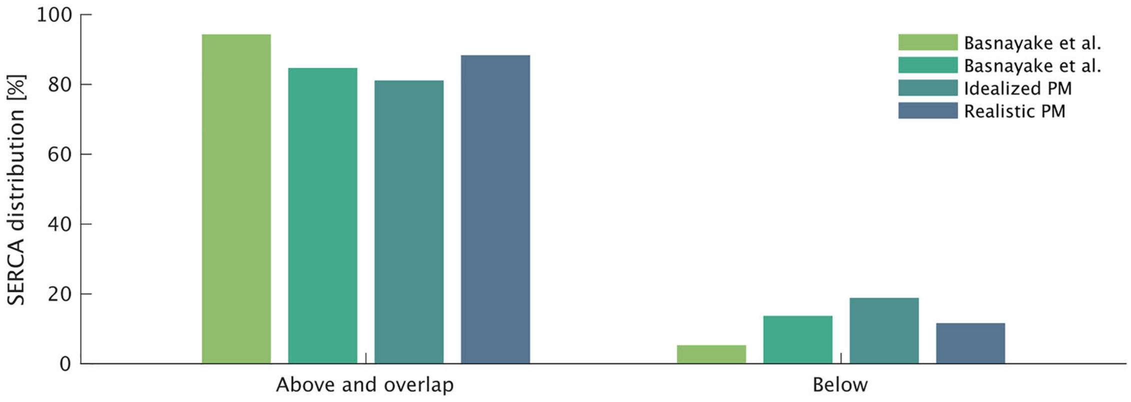

Figure 10. SERCA distribution within the spine apparatus compared to experimental data from Basnayake et al. (2019) with respect to synaptopodin, that is, the laminar region of the spine apparatus
Above and overlap refer to the laminar region of the spine apparatus, whereas below refers to all non-laminar regions of the SER.

of single spines (Obashi et al., 2021), we could not find any experiments related specifically to the gating of RyRs in these structures. Although we acknowledge that our simulations might not match the quantitative RyR opening probabilities measured in spines, our results give insights into the qualitative trends that different RyR distributions have on RyR opening probabilities. To account for this unknown related to realistic probability of RyR opening during a given stimulus event, we have divided the simulation result set **N** into two subsets **n** and **N****n**, those containing at least one open RyR throughout the simulation and that only have closed RyRs, respectively. This allows us to understand the effect of RyR opening independent of the RyR opening probability. Previous experimental studies have reported a contribution of RyR-mediated Ca^{2+} release to LTP (Raymond & Redman, 2002; Valdés-Undurraga et al., 2023; Wang et al., 1996). Furthermore a recent study has proposed that RyRs amplify Ca^{2+} signals generated at the dendritic spines following the stimulation of postsynaptic NMDA receptors (Emptage et al., 1999; Vega-Vásquez et al., 2022). The functional contribution of RyRs and CICR in spine calcium signalling has been the subject of considerable debate. Early studies, such as Emptage et al. (1999), supported a role for RyRs in amplifying postsynaptic calcium signals. However subsequent experimental work (Brünig et al., 2004; Sabatini et al., 2002) was not able to replicate this, suggesting that CICR and thus RyRs may not substantially contribute to postsynaptic calcium following NMDAR activation. More

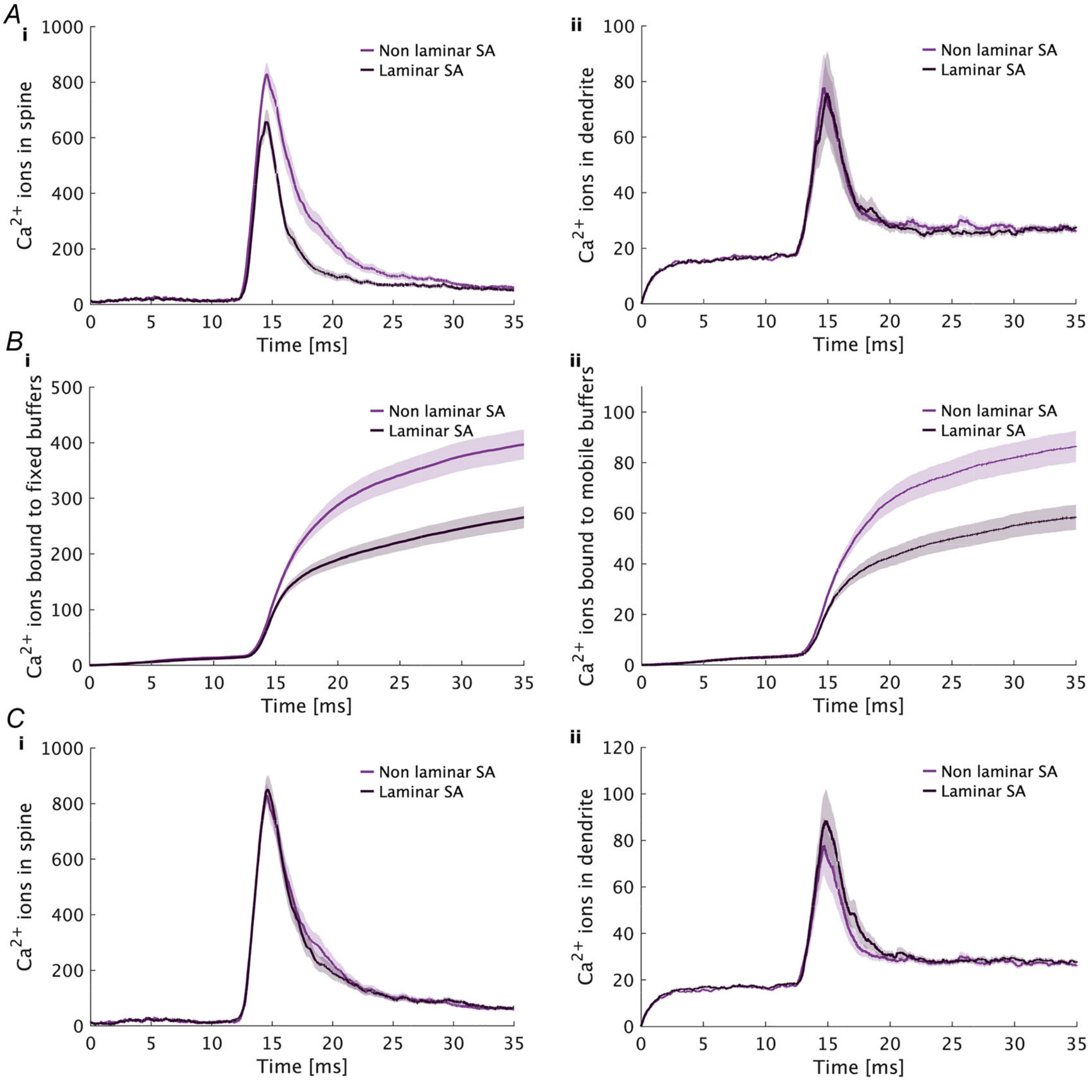

Figure 11. Comparison of effect of SERCA distribution an Ca^{2+} buffers in spine and dendrite
(A) Comparison between Ca^{2+} dynamics in an inactive ER (only SERCA) for both laminar and non-laminar ER. (B) Number of Ca^{2+} ions bound to fixed and mobile buffers in the inactive ER simulation set-up. (C) Ca^{2+} dynamics in an inactive ER (only SERCA) assuming constant number of SERCA.

recently it has been proposed that discrepancies in the functional role of RyRs may stem from differences in experimental conditions, particularly the developmental stage of the neuronal tissue used. For instance Lee et al. (2016) suggested that CICR could have a more prominent role during specific postnatal developmental periods. Given this ongoing debate, it is important to note that our study focuses on providing a computational framework to explore how ER and RyR distributions affect calcium dynamics and spine-to-dendrite communication. Although our simulations predict that RyRs could amplify calcium signals, as suggested by some experimental studies, we acknowledge that the true extent of their role in vivo remains unresolved.

Furthermore, it is likely that the quantitative opening probability of RyRs in spines is higher than those measured in our simulations. Nevertheless our results give new insights in understanding the effect of an active ER and RyRs on spine-to-dendrite Ca^{2+} communication. We were also unable to find any experimental data regarding the direct measurement of Ca^{2+} concentration within the SA. We chose an ER Ca^{2+} concentration of 150 μM as used in a previous computational model on cerebellar Purkinje cells (Doi et al., 2005), which used a value measured in mouse pancreatic acinar cells (Park et al., 2000). In cardiomyocytes, however, sarcoplasmic reticulum concentrations have been measured up to 1.2–1.8 mM (Wasserstrom et al., 2010). Due to the high variability in ER Ca^{2+} concentrations, further experimental investigation is required to constrain the values for Ca^{2+} concentration in dendritic spines. Furthermore, as shown by Dittmer et al. (2017), increased ER content could increase the Ca^{2+} storage capacity of spines, which is associated with large storing capacity of large spine volumes as observed during LTP. To study whether our choice of RyR concentration greatly impacted our results, we ran simulations with two further RyR concentrations. The results show higher Ca^{2+} reaching the dendrite at higher RyR concentrations as reported previously by Rosado et al. (2022) and also match the results shown in this paper; see Fig. 13.

Computational models help explore biophysical processes in dendritic spines over several timescales going from a few milliseconds (Bell et al., 2022; Breit et al., 2018; Basnayake et al., 2019) to several minutes (Bell & Rangamani, 2023; Mäki-Marttunen et al., 2020; Ohadi et al., 2019) of Ca^{2+} signalling. Our model shows how the interplay between NMDAR, VSCCs, ER geometry, RyR location, Ca^{2+} buffers and SERCA modulate Ca^{2+} dynamics and can have effects on downstream signalling and spine-to-dendrite communication. We note that our results are focused on early stage membrane depolarization stimulus and the impact of these effects should be studied for longer events, and high frequency stimulation of the spines (Dhanrajan et al., 2004; Zhu et al., 2015). It has been shown that Ca^{2+} influx through the L-type Ca^{2+} channels leads to further release of ER Ca^{2+} (Dittmer et al., 2019) at the timescale of several

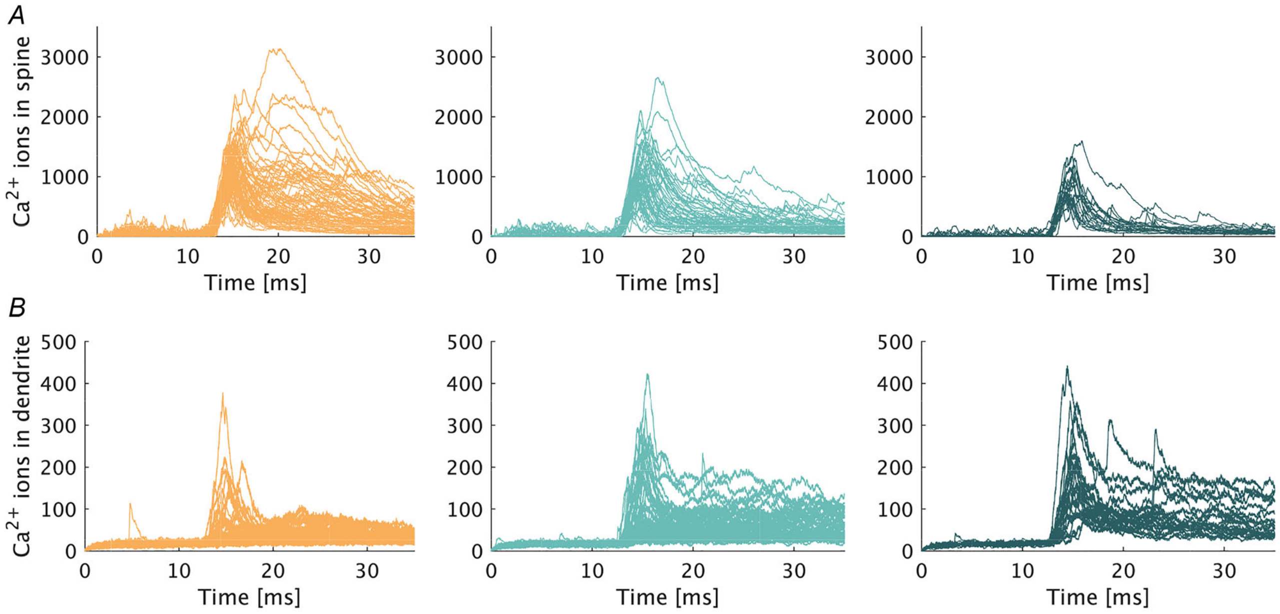

Figure 12. Individual Ca^{2+} sparks for each simulation assuming an idealized plasma membrane geometry
(A) Number of Ca^{2+} ions per individual simulation in the spine, shown for three RyR distributions: head (left), neck (centre) and low neck (right). (B) Number of Ca^{2+} ions per individual simulation in the dendrite, shown for three RyR distributions: head (left), neck (centre) and low neck (right).

seconds. Furthermore it has been recently reported that Ca^{2+} efflux from CICR mechanisms activates stromal interaction molecule 1 (STIM1) feedback inhibition of L-type Ca^{2+} channels (Dittmer et al., 2017, 2019). STIM1 activation also leads to the recruitment and gating of plasma membrane Ca^{2+} Orai1 channels (Hogan, 2015; Segal & Korkotian, 2016), allowing for further influx of Ca^{2+} through the plasma membrane. This process, known as SOCE, results in both cytoplasmic Ca^{2+} signalling and refilling of the internal Ca^{2+} stores (Basnayake et al., 2021; Hogan, 2015). Studies have shown that Orai1 channels induce local Ca^{2+} signals at long timescales (Basnayake et al., 2021; Lis et al., 2007; Mercer et al., 2006; Schober et al., 2019) on the order of several seconds, whereas our simulations focus on the timescale of 35 ms. We extended our ODE model to include SOCE. Although the results did not differ significantly from the original formulation, future studies with longer simulation events should include the crosstalk between ER, L-type Ca^{2+} channels, STIM1 and Orai1 to understand how RyR distribution and ER laminarity might affect the SOCE mechanism. Future studies should also investigate how

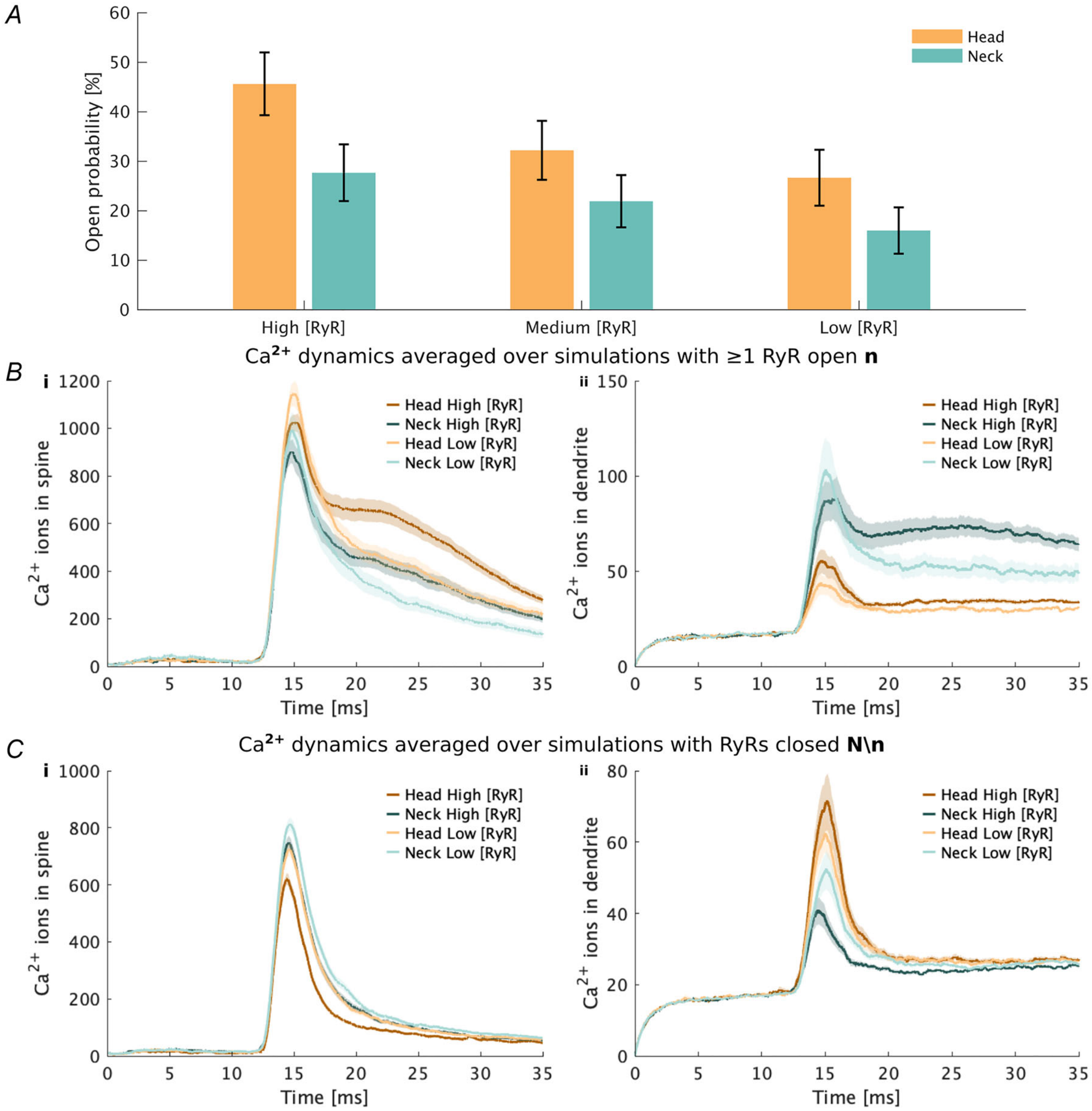

Figure 13. Effect of different RyR concentrations on Ca^{2+} dynamics when assuming a head and a neck distribution

(A) RyR opening probability when assuming a high, medium and low RyR concentration. (B) Ca^{2+} dynamics in the spine and dendrite averaged over simulations containing at least one open RyR **n**. Mean and standard error of the mean of all the simulations are shown. (C) Ca^{2+} dynamics in the spine and dendrite averaged over simulations where all RyRs remained closed **N****n**. Mean and standard error of the mean of all the simulations are shown.

our results affect other neuronal downstream signalling, such as the influence of Ca^{2+} on gene transcription at the nucleus (Bading, 2013) and other signalling pathways.

References

Alimohamadi, H., Bell, M. K., Halpain, S., & Rangamani, P. (2021). Mechanical principles governing the shapes of dendritic spines. *Frontiers in Physiology*, **12**, 657074.

Bading, H. (2013). Nuclear calcium signalling in the regulation of brain function. *Nature Reviews Neuroscience*, **14**(9), 593–608.

Barbara, J.-G. (2002). Ip3-dependent calcium-induced calcium release mediates bidirectional calcium waves in neurones: Functional implications for synaptic plasticity. *Biochimica et Biophysica Acta: Proteins and Proteomics*, **1600**(1-2), 12–18.

Bartol, T. M., Keller, D. X., Kinney, J. P., Bajaj, C. L., Harris, K. M., Sejnowski, T. J., & Kennedy, M. B. (2015). Computational reconstitution of spine calcium transients from individual proteins. *Frontiers in Synaptic Neuroscience*, **7**, 17.

Basnayake, K., Mazaud, D., Bemelmans, A., Rouach, N., Korkotian, E., & Holcman, D. (2019). Fast calcium transients in dendritic spines driven by extreme statistics. *PLoS Biology*, **17**(6), e2006202.

Basnayake, K., Mazaud, D., Kushnireva, L., Bemelmans, A., Rouach, N., Korkotian, E., & Holcman, D. (2021). Nanoscale molecular architecture controls calcium diffusion and ER replenishment in dendritic spines. *Science Advances*, **7**(38), eabh1376.

Bell, M., Bartol, T., Sejnowski, T., & Rangamani, P. (2019). Dendritic spine geometry and spine apparatus organization govern the spatiotemporal dynamics of calcium. *Journal of General Physiology*, **151**(8), 1017–1034.

Bell, M. K., Holst, M. V., Lee, C. T., & Rangamani, P. (2022). Dendritic spine morphology regulates calcium-dependent synaptic weight change. *Journal of General Physiology*, **154**(8), e202112980.

Bell, M. K., & Rangamani, P. (2023). Crosstalk between biochemical signalling network architecture and trafficking governs ampar dynamics in synaptic plasticity. *The Journal of Physiology* **601**, 3377–3402.

Benavides-Piccione, R., Regalado-Reyes, M., Fernaud-Espinosa, I., Kastanauskaite, A., Tapia-González, S., León-Espinosa, G., Rojo, C., Insausti, R., Segev, I., & DeFelipe, J. (2020). Differential structure of hippocampal ca1 pyramidal neurons in the human and mouse. *Cerebral Cortex*, **30**(2), 730–752.

Berridge, M. J. (1993). Inositol trisphosphate and calcium signalling. *Nature*, **361**(6410), 315–325.

Bhalla, U. S. (2004). Signaling in small subcellular volumes. II. Stochastic and diffusion effects on synaptic network properties. *Biophysical Journal*, **87**(2), 745–753.

Bourne, J. N., & Harris, K. M. (2008). Balancing structure and function at hippocampal dendritic spines. *Annual Review of Neuroscience*, **31**, 47–67.

Breit, M., Kessler, M., Stepniewski, M., Vlachos, A., & Queisser, G. (2018). Spine-to-dendrite calcium modeling discloses relevance for precise positioning of ryanodine receptor-containing spine endoplasmic reticulum. *Scientific Reports*, **8**(1), 1–17.

Brünig, I., Kaech, S., Brinkhaus, H., Oertner, T. G., & Matus, A. (2004). Influx of extracellular calcium regulates actin-dependent morphological plasticity in dendritic spines. *Neuropharmacology*, **47**(5), 669–676.

Chirillo, M. A., Waters, M. S., Lindsey, L. F., Bourne, J. N., & Harris, K. M. (2019). Local resources of polyribosomes and SER promote synapse enlargement and spine clustering after long-term potentiation in adult rat hippocampus. *Scientific Reports*, **9**(1), 3861.

Colgan, L. A., & Yasuda, R. (2014). Plasticity of dendritic spines: Subcompartmentalization of signaling. *Annual Review of Pysiology*, **76**, 365–385.

deSevilla, D. F., & Buno, W. (2010). The muscarinic long-term enhancement of NMDA and AMPA receptor-mediated transmission at Schaffer collateral synapses develop through different intracellular mechanisms. *Journal of Neuroscience*, **30**(33), 11032–11042.

deSevilla, D. F., Núnez, A., Borde, M., Malinow, R., & Buno, W. (2008). Cholinergic-mediated IP3-receptor activation induces long-lasting synaptic enhancement in CA1 pyramidal neurons. *Journal of Neuroscience*, **28**(6), 1469–1478.

De Young, G. W., & Keizer, J. (1992). A single-pool inositol 1, 4, 5-trisphosphate-receptor-based model for agonist-stimulated oscillations in Ca^{2+} concentration. *The Proceedings of the National Academy of Sciences*, **89**(20), 9895–9899.

Dhanrajan, T. M., Lynch, M. A., Kelly, A., Popov, V. I., Rusakov, D. A., & Stewart, M. G. (2004). Expression of long-term potentiation in aged rats involves perforated synapses but dendritic spine branching results from high-frequency stimulation alone. *Hippocampus*, **14**(2), 255–264.

Dittmer, P. J., Dell'Acqua, M. L., & Sather, W. A. (2019). Synaptic crosstalk conferred by a zone of differentially regulated Ca^{2+} signaling in the dendritic shaft adjoining a potentiated spine. *The Proceedings of the National Academy of Sciences*, **116**(27), 13611–13620.

Dittmer, P. J., Wild, A. R., Dell'Acqua, M. L., & Sather, W. A. (2017). STIM1 Ca^{2+} sensor control of L-type Ca^{2+}-channel-dependent dendritic spine structural plasticity and nuclear signaling. *Cell Reports*, **19**(2), 321–334.

Doi, T., Kuroda, S., Michikawa, T., & Kawato, M. (2005). Inositol 1, 4, 5-trisphosphate-dependent Ca^{2+} threshold dynamics detect spike timing in cerebellar Purkinje cells. *Journal of Neuroscience*, **25**(4), 950–961.

Ellisman, M. H., Deerinck, T. J., Ouyang, Y., Beck, C. F., Tanksley, S. J., Walton, P. D., Airey, J. A., & Sutko, J. L. (1990). Identification and localization of ryanodine binding proteins in the avian central nervous system. *Neuron*, **5**(2), 135–146.

Emptage, N., Bliss, T. V., & Fine, A. (1999). Single synaptic events evoke NMDA receptor–mediated release of calcium from internal stores in hippocampal dendritic spines. *Neuron*, **22**(1), 115–124.

Falahati, H., Wu, Y., Feuerer, V., Simon, H.-G., & De Camilli, P. (2022). Proximity proteomics of synaptopodin provides insight into the molecular composition of the spine apparatus of dendritic spines. *Proceedings of the National Academy of Sciences of the United States of America*, **119**(42), e2203750119.

Harris, K. M. (2020). Structural LTP: From synaptogenesis to regulated synapse enlargement and clustering. *Current Opinion in Neurobiology*, **63**, 189–197.

Harris, K. M., Jensen, F. E., & Tsao, B. (1992). Three-dimensional structure of dendritic spines and synapses in rat hippocampus (CA1) at postnatal day 15 and adult ages: Implications for the maturation of synaptic physiology and long-term potentiation. *Journal of Neuroscience*, **12**(7), 2685–2705.

Hernandez Mesa, M., McCabe, K., & Rangamani, P. (2025). Synaptic cleft geometry modulates NMDAR opening probability by tuning neurotransmitter residence time. *Biophysical Journal*, **124**(7), 1058–1072.

HernándezMesa, M., van den Brink, J., Louch, W. E., McCabe, K. J., & Rangamani, P. (2022). Nanoscale organization of ryanodine receptor distribution and phosphorylation pattern determines the dynamics of calcium sparks. *PLOS Computational Biology*, **18**(6), 1–22.

Hetz, C., & Mollereau, B. (2014). Disturbance of endoplasmic reticulum proteostasis in neurodegenerative diseases. *Nature Reviews Neuroscience*, **15**(4), 233–249.

Higley, M. J., & Sabatini, B. L. (2012). Calcium signaling in dendritic spines. *Cold Spring Harbor Perspectives in Biology*, **4**(4), a005686.

Hogan, P. G. (2015). The STIM1–ORAI1 microdomain. *Cell Calcium*, **58**(4), 357–367.

Holcman, D., Schuss, Z., & Korkotian, E. (2004). Calcium dynamics in dendritic spines and spine motility. *Biophysical Journal*, **87**(1), 81–91.

Hou, Y., Bai, J., Shen, X., de Langen, O., Li, A., Lal, S., Dos Remedios, C. G., Baddeley, D., Ruygrok, P. N., Soeller, C., & Crossman, D. J. (2021). Nanoscale organisation of ryanodine receptors and Junctophilin-2 in the failing human heart. *Frontiers in Physiology*, **12**, 724372.

Husar, A., Ordyan, M., Garcia, G. C., Yancey, J. G., Saglam, A. S., Faeder, J. R., Bartol, T. M., & Sejnowski, T. J. (2022). MCell4 with BioNetGen: A Monte Carlo simulator of rule-based reaction-diffusion systems with Python interface. *bioRxiv*, 2022-05. https://doi.org/10.1101/2022.05.17.492333

Inc, T. M. (2022). *Matlab version: 9.13.0 (r2022b)*. https://www.mathworks.com

Jedlicka, P., Vlachos, A., Schwarzacher, S. W., & Deller, T. (2008). A role for the spine apparatus in LTP and spatial learning. *Behavioural Brain Research*, **192**(1), 12–19.

Jonas, P., Major, G., & Sakmann, B. (1993). Quantal components of unitary EPSCs at the mossy fibre synapse on CA3 pyramidal cells of rat hippocampus. *The Journal of Physiology*, **472**(1), 615–663.

Kim, B., Hawes, S. L., Gillani, F., Wallace, L. J., & Blackwell, K. T. (2013). Signaling pathways involved in striatal synaptic plasticity are sensitive to temporal pattern and exhibit spatial specificity. *PLoS Computational Biology*, **9**(3), e1002953.

Kolstad, T. R., van den Brink, J., MacQuaide, N., Lunde, P. K., Frisk, M., Aronsen, J. M., Norden, E. S., Cataliotti, A., Sjaastad, I., Sejersted, O. M., Edwards, A. G., Lines, G. T., & & Louch, W. E. (2018). Ryanodine receptor dispersion disrupts Ca^{2+} release in failing cardiac myocytes. *eLife*, **7**, e39427.

Konietzny, A., Wegmann, S., & Mikhaylova, M. (2022). The endoplasmic reticulum puts a new spin on synaptic tagging. *Trends in Neurosciences* **46**, 32–44.

Korkotian, E., & Segal, M. (2011). Synaptopodin regulates release of calcium from stores in dendritic spines of cultured hippocampal neurons. *The Journal of Physiology*, **589**(24), 5987–5995.

Kotaleski, J. H., & Blackwell, K. T. (2010). Modelling the molecular mechanisms of synaptic plasticity using systems biology approaches. *Nature Reviews Neuroscience*, **11**(4), 239–251.

Lam, A. K., & Galione, A. (2013). The endoplasmic reticulum and junctional membrane communication during calcium signaling. *Biochimica et Biophysica Acta: Molecular Cell Research*, **1833**(11), 2542–2559.

Lee, C. T., Laughlin, J. G., Angliviel de La Beaumelle, N., Amaro, R. E., McCammon, J. A., Ramamoorthi, R., Holst, M., & Rangamani, P. (2020). 3D mesh processing using GAMer 2 to enable reaction-diffusion simulations in realistic cellular geometries. *PLoS Computational Biology*, **16**(4), e1007756.

Lee, K. F., Soares, C., Thivierge, J.-P., & Béïque, J.-C. (2016). Correlated synaptic inputs drive dendritic calcium amplification and cooperative plasticity during clustered synapse development. *Neuron*, **89**(4), 784–799.

Leung, A., Ohadi, D., Pekkurnaz, G., & Rangamani, P. (2021). Systems modeling predicts that mitochondria ER contact sites regulate the postsynaptic energy landscape. *Nature Partner Journals Systems Biology and Applications*, **7**(1), 26.

Lis, A., Peinelt, C., Beck, A., Parvez, S., Monteilh-Zoller, M., Fleig, A., & Penner, R. (2007). CRACM1, CRACM2, and CRACM3 are store-operated Ca^{2+} channels with distinct functional properties. *Current Biology*, **17**(9), 794–800.

Magee, J. C., & Johnston, D. (1995). Characterization of single voltage-gated Na+ and Ca^{2+} channels in apical dendrites of rat CA1 pyramidal neurons. *The Journal of Physiology*, **487**(1), 67–90.

Magee, J. C., & Johnston, D. (1997). A synaptically controlled, associative signal for Hebbian plasticity in hippocampal neurons. *Science*, **275**(5297), 209–213.

Mäki-Marttunen, T., Iannella, N., Edwards, A. G., Einevoll, G. T., & Blackwell, K. T. (2020). A unified computational model for cortical post-synaptic plasticity. *eLife*, **9**, e55714.

Matsuzaki, M., Honkura, N., Ellis-Davies, G. C., & Kasai, H. (2004). Structural basis of long-term potentiation in single dendritic spines. *Nature*, **429**(6993), 761–766.

McPherson, P., & Campbell, K. (1993). Characterization of the major brain form of the ryanodine receptor/Ca^{2+} release channel. *Journal of Biological Chemistry*, **268**(26), 19785–19790.

McPhersonx, P. S., Kim, Y.-K., Valdivia, H., Knudson, C. M., Takekura, H., Franzini-Armstrong, C., Coronadot, R., & Campbell, K. P. (1991). The brain ryanodine receptor: A caffeine-sensitive calcium release channel. *Neuron*, **7**(1), 17–25.

Means, S., Smith, A. J., Shepherd, J., Shadid, J., Fowler, J., Wojcikiewicz, R. J., Mazel, T., Smith, G. D., & Wilson, B. S. (2006). Reaction diffusion modeling of calcium dynamics with realistic ER geometry. *Biophysical Journal*, **91**(2), 537–557.

Mercer, J. C., DeHaven, W. I., Smyth, J. T., Wedel, B., Boyles, R. R., Bird, G. S., & Putney, J. W. (2006). Large store-operated calcium selective currents due to co-expression of Orai1 or Orai2 with the intracellular calcium sensor, Stim1. *Journal of Biological Chemistry*, **281**(34), 24979–24990.

Musall, S. (2023). *stdshade*. MATLAB Central File Exchange. Retrieved August 1, from https://www.mathworks.com/matlabcentral/fileexchange/29534-stdshade

Nimchinsky, E. A., Sabatini, B. L., & Svoboda, K. (2002). Structure and function of dendritic spines. *Annual Review of Physiology*, **64**(1), 313–353.

Obashi, K., Taraska, J. W., & Okabe, S. (2021). The role of molecular diffusion within dendritic spines in synaptic function. *Journal of General Physiology*, **153**(4), e202012814.

Ohadi, D., Schmitt, D. L., Calabrese, B., Halpain, S., Zhang, J., & Rangamani, P. (2019). Computational modeling reveals frequency modulation of calcium-cAMP/PKA pathway in dendritic spines. *Biophysical Journal*, **117**(10), 1963–1980.

Ornelas-Guevara, R., Gil, D., Voorsluijs, V., & Dupont, G. (2023). Computational investigation of IP3 diffusion. *Scientific Reports*, **13**(1), 2922.

Park, M. K., Petersen, O. H., & Tepikin, A. V. (2000). The endoplasmic reticulum as one continuous Ca^{2+} pool: Visualization of rapid Ca^{2+} movements and equilibration. *The European Molecular Biology Organization Journal*, **19**(21), 5729–5739.

Perez-Alvarez, A., Yin, S., Schulze, C., Hammer, J. A., Wagner, W., & Oertner, T. G. (2020). Endoplasmic reticulum visits highly active spines and prevents runaway potentiation of synapses. *Nature Communications*, **11**(1), 5083.

Rangamani, P., Levy, M. G., Khan, S., & Oster, G. (2016). Paradoxical signaling regulates structural plasticity in dendritic spines. *Proceedings of the National Academy of Sciences of the United States of America*, **113**(36), E5298–E5307.

Raymond, C. R., & Redman, S. J. (2002). Different calcium sources are narrowly tuned to the induction of different forms of LTP. *Journal of Neurophysiology*, **88**(1), 249–255.

Regehr, W. G., & Tank, D. W. (1990). Postsynaptic NMDA receptor-mediated calcium accumulation in hippocampal CAl pyramidal cell dendrites. *Nature*, **345**(6278), 807–810.

Resasco, D. C., Gao, F., Morgan, F., Novak, I. L., Schaff, J. C., & Slepchenko, B. M. (2012). Virtual cell: Computational tools for modeling in cell biology. *Wiley Interdisciplinary Reviews: Systems Biology and Medicine*, **4**(2), 129–140.

Rosado, J., Bui, V. D., Haas, C. A., Beck, J., Queisser, G., & Vlachos, A. (2022). Calcium modeling of spine apparatus-containing human dendritic spines demonstrates an “all-or-nothing” communication switch between the spine head and dendrite. *PLoS Computational Biology*, **18**(4), e1010069.

Sabatini, B. L., Oertner, T. G., & Svoboda, K. (2002). The life cycle of Ca^{2+} ions in dendritic spines. *Neuron*, **33**(3), 439–452.

Saftenku, E. (2022). Simulation of store-operated calcium entry in neurons. *Neurophysiology*, **54**(1), 14–24.

Schober, R., Waldherr, L., Schmidt, T., Graziani, A., Stilianu, C., Legat, L., Groschner, K., & Schindl, R. (2019). STIM1 and Orai1 regulate Ca^{2+} microdomains for activation of transcription. *Biochimica et Biophysica Acta: Molecular Cell Research*, **1866**(7), 1079–1091.

Schwaller, B. (2010). Cytosolic Ca^{2+} buffers. *Cold Spring Harbor Perspectives in Biology*, **2**(11), a004051.

Segal, M., & Korkotian, E. (2014). Endoplasmic reticulum calcium stores in dendritic spines. *Frontiers in Neuroanatomy*, **8**, 64.

Segal, M., & Korkotian, E. (2016). Roles of calcium stores and store-operated channels in plasticity of dendritic spines. *The Neuroscientist*, **22**(5), 477–485.

Segal, M., Vlachos, A., & Korkotian, E. (2010). The spine apparatus, synaptopodin, and dendritic spine plasticity. *The Neuroscientist*, **16**(2), 125–131.

Sharp, A. H., McPherson, P. S., Dawson, T. M., Aoki, C., Campbell, K. P., & Snyder, S. H. (1993). Differential immunohistochemical localization of inositol 1, 4, 5-trisphosphate and ryanodine-sensitive Ca^{2+} release channels in rat brain. *Journal of Neuroscience*, **13**(7), 3051–3063.

Shen, X., van den Brink, J., Hou, Y., Colli, D., Le, C., Kolstad, T. R., MacQuaide, N., Carlson, C. R., Kekenes-Huskey, P. M., Edwards, A. G., Soeller, C., & Louch, W. (2019). 3D dSTORM imaging reveals novel detail of ryanodine receptor localization in rat cardiac myocytes. *The Journal of Physiology*, **597**(2), 399–418.

Singh, N., Bartol, T., Levine, H., Sejnowski, T., & Nadkarni, S. (2021). Presynaptic endoplasmic reticulum regulates short-term plasticity in hippocampal synapses. *Communications Biology*, **4**(1), 1–13.

Spacek, J., & Harris, K. M. (1997). Three-dimensional organization of smooth endoplasmic reticulum in hippocampal CA1 dendrites and dendritic spines of the immature and mature rat. *Journal of Neuroscience*, **17**(1), 190–203.

Stern, M. D., Song, L.-S., Cheng, H., Sham, J. S., Yang, H. T., Boheler, K. R., & Ríos, E. (1999). Local control models of cardiac excitation–contraction coupling: A possible role for allosteric interactions between ryanodine receptors. *The Journal of General Physiology*, **113**(3), 469–489.

Tanskanen, A. J., Greenstein, J. L., Chen, A., Sun, S. X., & Winslow, R. L. (2007). Protein geometry and placement in the cardiac dyad influence macroscopic properties of calcium-induced calcium release. *Biophysical Journal*, **92**(10), 3379–3396.

Valdés-Undurraga, I., Lobos, P., Sánchez-Robledo, V., Arias-Cavieres, A., SanMartín, C. D., Barrientos, G., More, J., Muñoz, P., Paula-Lima, A. C., Hidalgo, C., & Adasme, T. (2023). Long-term potentiation and spatial memory training stimulate the hippocampal expression of RyR2 calcium release channels. *Frontiers in Cellular Neuroscience*, **17**, 1132121.

Van Harreveld, A., & Fifkova, E. (1975). Swelling of dendritic spines in the fascia dentata after stimulation of the perforant fibers as a mechanism of post-tetanic potentiation. *Experimental Neurology*, **49**(3), 736–749.

Vargas-Caballero, M., & Robinson, H. P. (2004). Fast and slow voltage-dependent dynamics of magnesium block in the NMDA receptor: The asymmetric trapping block model. *Journal of Neuroscience*, **24**(27), 6171–6180.

Vega-Vásquez, I., Lobos, P., Toledo, J., Adasme, T., Paula-Lima, A., & Hidalgo, C. (2022). Hippocampal dendritic spines express the RyR3 but not the RyR2 ryanodine receptor isoform. *Biochemical and Biophysical Research Communications*, **633**, 96–103.

Vlachos, A., Korkotian, E., Schonfeld, E., Copanaki, E., Deller, T., & Segal, M. (2009). Synaptopodin regulates plasticity of dendritic spines in hippocampal neurons. *Journal of Neuroscience*, **29**(4), 1017–1033.

Walton, P. D., Airey, J. A., Sutko, J. L., Beck, C. F., Mignery, G. A., Südhof, T. C., Deerinck, T. J., & Ellisman, M. H. (1991). Ryanodine and inositol trisphosphate receptors coexist in avian cerebellar Purkinje neurons. *The Journal of Cell Biology*, **113**(5), 1145–1157.

Wang, S. Q., Stern, M. D., Ríos, E., & Cheng, H. (2004). The quantal nature of Ca^{2+} sparks and in situ operation of the ryanodine receptor array in cardiac cells. *Proceedings of the National Academy of Sciences*, **101**(11), 3979–3984.

Wang, Y., Wu, J., Rowan, M. J., & Anwyl, R. (1996). Ryanodine produces a low frequency stimulation-induced NMDA receptor-independent long-term potentiation in the rat dentate gyrus in vitro. *The Journal of Physiology*, **495**(3), 755–767.

Wasserstrom, J. A., Shiferaw, Y., Chen, W., Ramakrishna, S., Patel, H., Kelly, J. E., O'Toole, M. J., Pappas, A., Chirayil, N., Bassi, N., Akintilo, L., Wu, M., Arora, R., & Aistrup, G. L. (2010). Variability in timing of spontaneous calcium release in the intact rat heart is determined by the time course of sarcoplasmic reticulum calcium load. *Circulation Research*, **107**(9), 1117–1126.

Wenthold, R. J., Petralia, R. S., Blahos, J. I. I., & Niedzielski, A. (1996). Evidence for multiple AMPA receptor complexes in hippocampal CA1/CA2 neurons. *Journal of Neuroscience*, **16**(6), 1982–1989.

Wu, Y., Whiteus, C., Xu, C. S., Hayworth, K. J., Weinberg, R. J., Hess, H. F., & De Camilli, P. (2017). Contacts between the endoplasmic reticulum and other membranes in neurons. *Proceedings of the National Academy of Sciences of the United States of America*, **114**(24), E4859–E4867.

Yang, G., Pan, F., & Gan, W.-B. (2009). Stably maintained dendritic spines are associated with lifelong memories. *Nature*, **462**(7275), 920–924.

Yasuda, R., Sabatini, B. L., & Svoboda, K. (2003). Plasticity of calcium channels in dendritic spines. *Nature Neuroscience*, **6**(9), 948–955.

Yuste, R., & Denk, W. (1995). Dendritic spines as basic functional units of neuronal integration. *Nature*, **375**(6533), 682–684.

Zhu, G., Liu, Y., Wang, Y., Bi, X., & Baudry, M. (2015). Different patterns of electrical activity lead to long-term potentiation by activating different intracellular pathways. *Journal of Neuroscience*, **35**(2), 621–633.

Additional information

Data availability statement

The Python code for running simulations will be available on GitHub upon publication at https://github.com/RangamaniLabUCSD/SpineApparatus.git. To run the simulations, MCell should be downloaded from https://mcell.org.

Competing interests

P.R. is a consultant for Simula Research Laboratories in Oslo, Norway and receives income. The terms of this arrangement have been reviewed and approved by the University of California, San Diego in accordance with its conflict-of-interest policies. Other authors declare no competing interests.

Author contributions

M.H.M. contributed to the conceptualization of the study, performed simulations and data analysis, prepared the figures and drafted the manuscript. G.C.G. contributed to the design of the study, supervised the data interpretation and was involved in revising the manuscript critically for important intellectual content. F.J.H. contributed to the conceptualization of the study and helped in editing the manuscript. K.J.M. contributed to the conceptualization of the study, provided supervision, acquired funding for the project and contributed to the final editing and approval of the manuscript. P.R. contributed to the conceptualization of the study, provided supervision, acquired funding for the project and contributed to the final editing and approval of the manuscript. All authors contributed to either the conception or design of the work, or the acquisition, analysis or interpretation of data. All authors also participated in drafting the manuscript or revising it critically for important intellectual content. All authors have approved the final version of the manuscript and agree to be accountable for all aspects of the work. All persons designated as authors qualify for authorship, and all those who qualify for authorship are listed.

Funding

M.H.M. and K.J.M. are supported by the Simula–UCSD–University of Oslo Research and PhD training (SUURPh) program, an international collaboration in computational biology and medicine funded by the Norwegian Ministry of Education and Research. F.J.H. is supported by NIH grant NINDS NS115947. This work was supported in part by Air Force Office of Scientific Research (AFOSR) MURI FA9550-18- 1-0051 to P.R.

Acknowledgements

We thank Emmet Francis, Ali Khalilimeybodi and Michael Tamkun for proofreading the manuscript and also for their valuable comments. VCell is supported by NIH Grant Number R24 GM134211 from the National Institute for General Medical Sciences. MCell development is supported by the NIGMS-funded (P41GM103712) National Center for Multiscale Modeling of Biological Systems (MMBioS). The simulations were in part performed on resources provided by Sigma2 – the National Infrastructure for High Performance Computing and Data Storage in Norway.

Keywords

calcium dynamics, dendritic spines, NMDARs, spine apparatus

Supporting information

Additional supporting information can be found online in the Supporting Information section at the end of the HTML view of the article. Supporting information files available:

Peer Review History
Figure R1
Figure R2
Figure R3
Figure R1
Figure R2
Figure R3
Data S1
Figure S1
Figure S2
Figure S3
Figure S4